Radio-Source Tracker: Autonomous Attitude Determination on a Radio Interferometric Swarm

E. Rouillé[1], B. Cecconi[1], B. Segret[2], and J. N. Girard[1]

[1]LESIA, Observatoire de Paris, Université PSL, Sorbonne Université, Université Paris Cité, CNRS, Meudon, France
[2]CENSUS, Observatoire de Paris, Université PSL, Meudon, France

Key Points:

- Adaptation of star-tracker technique to an autonomous radio interferometric swarm
- Evaluated with a simulation pipeline in the context of a swarm of 50 nanosatellite over 100 km and for frequencies below 1 MHz
- Accuracy on the directional information expected better than 1 arcmin

Corresponding author: Erwan Rouillé, `erwan.rouille@obspm.fr`

Abstract

The development of satellite swarm technology offers new possibilities for space studies and comes with new challenges. Among them is the need of knowledge on the swarm topology and attitude, especially in the context of space-borne radio interferometry. This paper presents an algorithm that recovers the absolute swarm attitude autonomously.This algorithm uses the imaging capability of a low frequency radio interferometer that acts as a star-tracker using the main radio sources in the sky. The *Lost-In-Space* (LIS) mode is presented in this paper. This algorithm is studied through numerical simulations. This concept is applied here to the kilometric wavelength spectral range (30 kHz – 1 MHz) but the technique can be extended to higher frequencies.

Images are reconstructed using an iterative Discrete Fourier Transform (DFT) at two frequencies and using source subtractions. Pattern-matching is performed with a voting system implemented on geometrical parameters defined by triangles of sources. The radio sky in the working band is modeled by extrapolating down observation of the sky at 50 MHz. The modeled interferometer corresponds to the NOIRE (*Nanosatellite pour un Observatoire Interferométrique Radio dans l'Espace*) concept study. The accuracy on the recovered swarm attitude is measured for different levels of noise in the interferometric visibilities.

The simulation shows that, the suggested algorithm can achieve an attitude knowledge error lower than 1 arcmin for a swarm scale of 100 km. The requirements in terms of memory and computation capability are discussed as well as the limitations of the technique and the simulation.

1 Introduction

1.1 Context

The radio sky below 30 MHz remains mostly unexplored while it still holds essential information on the close and distant universe. Fields like stellar physics, planetary science or cosmology would benefit from observations in this frequency range (Cecconi et al., 2018; Cong et al., 2022). Indeed, ground-based astronomical observations at these long wavelengths are severely limited by Earth's ionospheric distortions below 50 MHz and complete reflection of radio waves below 10 MHz (de Gasperin, F. et al., 2018). In addition to ionospheric distortion, man-made strong transmitter Radio Frequency Interferences (RFI) signals below 30 MHz also impede observations. Thus, several space missions have been launched to explore this frequency range. The first one, RAE-B, has highlighted that the far-side of the Moon is a quiet place for radio astronomy, spared from Earth's radio emission (Alexander et al., 1975). This explains why space missions currently studied in this frequency range aim to be located around the Moon to benefit for its physical shielding effect. The recent history of space-based radio observatory studies is summarized in Table 1. Several of these mission studies anticipate a few tens of nodes which give them imaging capabilities through interferometric measurements.

For radio interferometers located at Earth orbit, the location of the satellites, and by extension the orientation of the swarm, as a single body, can be accurately computed using GNSS (Global Navigation Satellite Systems) measurements (Stuart et al., 2017). However, when it comes to a swarm of satellites located around the Moon or deeper in space, this technique no longer holds. A solution to this problem would be to use nearby reference beacons that can communicate with the nodes. For now, such beacons do not exist. The problem of autonomous absolute swarm attitude measurement has not been addressed in the literature so far. The present study looks into this problem by proposing a method that only requires radio interferometric measurements. To that extent, it

Name	Frequency (MHz)	Baseline (km)	# S/C	Location	Team or Country
SIRA	0.03 – 15	>10	12 – 16	Sun-Earth L1 halo	NASA/GSFC (2004)
SOLARA /SARA	0.1 – 10	<10000	20	Earth-Moon L1	NASA/JPL - MIT (2012)
OLFAR	0.03 – 30	∼100	50	Lunar orbit or Sun-Earth L4-L5	ASTRON/Delft, NL (2009)
DARIS	1 – 10	<100	9	Dynamic Solar Orbit	ASTRON/Nijmegen, NL
DEX	0.1 – 80	∼1	10^5	Sun-Earth L2	ESA-L2/L3 call
SURO	0.1 – 30	∼30	8	Sun-Earth L2	ESA M3 call
SULFRO	1 – 100	<30	12	Sun-Earth L2	NL-FR-China (2012)
DSL	0.1 – 50	<100	8	Lunar Orbit (linear array)	ESA-S2 (2015)
DEX2	0.1 – 80	100	10 – 100	Lunar Array	ESA-M5 (2016)
SunRISE	0.1 – 25	12	6	GEO graveyard	NASA mission (launched planned in 2023)

Table 1: Recent history of space-based radio observatory studies, adapted from (Cecconi et al., 2018).

does not require external supporting infrastructure. The algorithm is called "Radio Source Tracker" or *RST* algorithm.

Meanwhile, this technique relies on the satellites being able to run the algorithm on-board. Although this is still an emerging technology, the progress made signal processing miniaturization suggests that this could be feasible in the coming years.

1.2 Swarm Orientation and Interferometric Configuration

1.2.1 Interferometric Configuration

A radio interferometer is an observing system producing correlation coefficients (named "interferometric visibilities") from individual antenna signals. The collection of these coefficients can be used for reconstructing images in any observation direction in its individual antenna field of view. In the low frequency range, antennas are usually long dipoles that provide large beaming pattern that covers a large fraction of the sky. As a consequence, the antennas are usually not physically pointed to the direction of the observation, but rather electronically or digitally phased in groups into that direction.

The accuracy on the direction of observation relies on the accuracy on the attitude knowledge of the interferometer's baselines (i.e., the set of vectors joining each pair of nodes of the interferometer). In other words, errors on the attitude knowledge will propagate to the image domain as a bias in astrometry.

Nevertheless, directional information of scientific interferometric images can be recalibrated during post-processing. Nonetheless, accuracy on the attitude knowledge is required to make sure that all sources of interest appear in the images, and also to prevent the sources from being too far from the phase center.

Producing a directional information with an interferometer requires to tune a shift function and adjust it to an absolute direction of the sky. This requires the knowledge of the absolute orientation of the interferometric baselines. The absolute orientation of each individual node can be measured using a classical star-tracker, but retrieving its

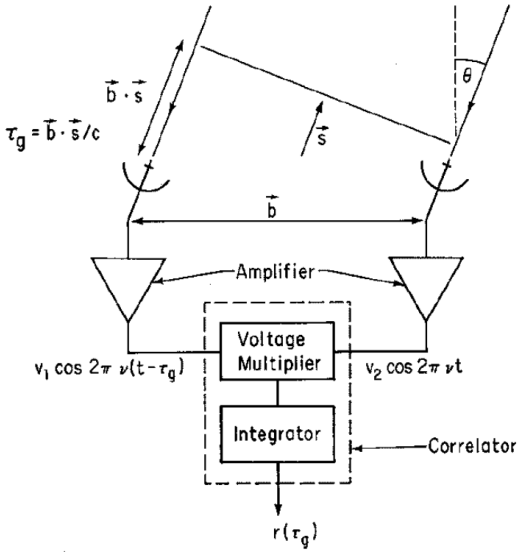

Figure 1: Simplified schematic diagram of a two-element interferometer. Source: Taylor et al. (1999).

location relative to its neighbors (i.e., retrieving the absolute orientation of the interferometric baselines) is a non-trivial problem.

The nodes have to be phased according to a given direction of observation in order to combine their signals. For a given pair of nodes, the phasing compensates the receiving time delay between the nodes due to the difference of distance in their optical path. This delay is expressed as $\tau_g = (\vec{b}_{i,j} \cdot \vec{s})/c$ where c is the speed of light, $\vec{s}$ is the unit vector corresponding to the pointing direction and $\vec{b}_{i,j} = \vec{r}_i - \vec{r}_j$ is the baseline between the position of the two nodes. These elements are depicted on Fig. 1. For a given frequency ν, this delay can be expressed as a phase shift. Its expression in the complex notation is $\exp(-\iota\vec{k} \cdot \vec{b})$ with the wave vector $\vec{k} = 2\pi\nu/c \cdot \vec{s}$ and where ι is the imaginary unit. Hence, the phase shift to be applied for an observation direction $\vec{s}$ depends on the baseline $\vec{b}$.

1.2.2 Consequence on Swarm Orientation

In the case of an autonomous swarm of satellites, the interferometer has to recover the baseline vectors on its own. The distances between the satellites can be precisely measured using techniques such as the time difference of arrival (TDoA) (Gustafsson & Gunnarsson, 2003). These measurements only give access to the norm $\|\vec{b}\|$ of the baselines. Here, reconstruction algorithms can be used to retrieve the topology of the swarm using only the distances. Such algorithms have already been developed (Chu & Chen, 2018; Rajan & van der Veen, 2015; Duisterwinkel et al., 2018) and can be used to determine the full set of relative baseline orientations. Yet, the computed vectors $\vec{b}$ are not provided in an absolute frame. They are expressed in a local frame generated by the topology reconstruction algorithm. This frame is hereafter referred to as the *system frame* and is noted $\mathcal{R}_s$.

In order to compute the delay τ_g, the direction $\vec{s}$ and the baselines $\vec{b}$ have to be expressed in the same frame. The direction $\vec{s}$ corresponds to the region of interest in the sky and is generally expressed in an inertial frame (such as the EME J2000 frame), which is hereafter referred to as the *absolute frame* and is noted $\mathcal{R}_a$. Interferometric imaging

requires the knowledge of: (a) the topology of the swarm and (b) the absolute attitude of the swarm. The knowledge of the swarm location is not required when parallax effects are neglected. Hence, retrieving the swarm attitude comes down to finding the transform between $\mathcal{R}_a$ and $\mathcal{R}_s$, which is noted $\boldsymbol{\mathcal{M}}$. This transform is a rotation, possibly combined with a planar reflection (in case the reconstructed topology is flipped with respect to the actual topology).

Even if this transform is unknown, the interferometer can still produce images of the sky but is unable to provide absolute directional information with it. The image will be the actual image of the full sky but rotated and possibly flipped with respect to reality. Thus, by comparing this image to the one expected in the absolute frame, it is possible to determine the transform matrix.

The efficiency of the *RST* algorithm is studied with a simulation pipeline that runs the algorithm with modeled inputs and by evaluating its outputs with a metric. The individual functions are not evaluated on their own, nor they are compared to other methods performing the same functions. Only the outputs of the *RST* algorithm are evaluated.

1.3 Framework

The study presented here is conducted in the framework of NOIRE — *Nanosatellites pour un Observatoire Interferométrique Radio dans l'Espace* (nanosatellites for an interferometric radio astronomy observatory in space), (Cecconi et al., 2018). This project is characterized by the number of nodes of the swarm $N_{sat} = 50$ and its maximum baseline $D_{max} = 100$ km. If the satellites are randomly arranged, they form $N_{bl} = N_{sat}(N_{sat}-1)/2 = 1225$ independent baselines. Each satellite is equipped with three orthogonal dipole antennas, which lengths are $L = 5$ m tip-to-tip.

Such a set of antennas can be considered as an isotropic antenna tripole when combined and used in their *short antenna regime* (i.e., when $\lambda \gg L$, that is frequencies below ~ 3 MHz in this case) (see Appendix B for details). This consideration reflect the way the antennas are expected to perform but is also a requirement for the *RST* function as explained in section 2.2.5.

This study assumes various simplifications that are listed below:

- The interferometer is assumed to be static. This hypothesis is valid when the acquisition time is very small compared to the orbital period. It means that the satellites relative velocities and individual spins can be neglected. Also, the Doppler effect can be neglected (see Appendix E).
- All effects due to frequency smearing are neglected.
- Also, it is assumed that: the clocks have no bias; the relative baselines' vectors are perfectly measured; all sources are in the far field.

2 Radio Source Tracker Algorithm

2.1 Principle

The main idea of the proposed algorithm is to use the images generated by the interferometer to compute its attitude on board like a star-tracker would, but in the radio domain. Several sources are detected and located in the reconstructed image and are then cross-matched with a list of known sources positions called the catalog. Without prior knowledge of the source label, the relative geometry between the sources are compared to that of the catalog. Once similar patterns of sources are recognized between the detected and reference source list, it is possible to assign the source Id and to compare the position of the detected sources to those tabulated in the catalog. Then, the

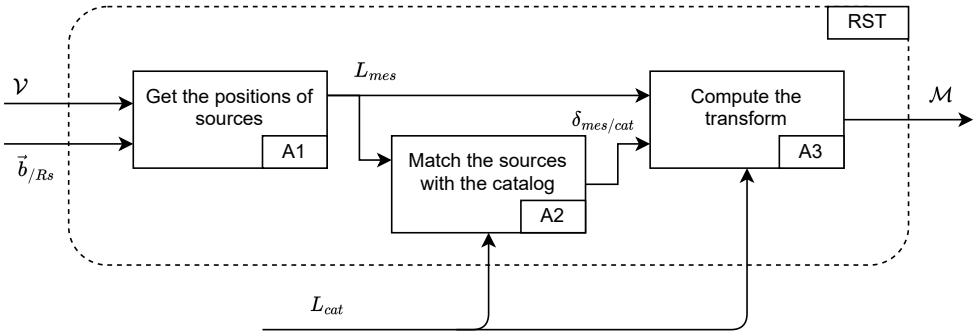

Figure 2: Main functions to be performed by the *RST* algorithm organized as an SADT (Structured Analysis and Design Technique) diagram.

geometric operations that transform the reference positions to the observed one can be computed and determines the swarm orientation. The main function of the *RST* algorithm are listed below and illustrated in Fig. 2:

1. Get the positions of the sources (A1)
2. Cross-match the sources with the catalog (A2)
3. Compute the transform (A3)

The visibilities and the relative baselines are supposed to be known priors at the beginning of the algorithm. The next steps are described in the following subsections.

The algorithm is meant to retrieve the attitude of the swarm at quite a high rate (depending on the orbital parameters), therefore it has to be run quickly and locally. Thus, it cannot be computed to the ground due to telecommunications delays.

2.2 Get the Position of the Sources: Function A1

The purpose of this function is to return a list of source positions L_{mes}. Similarly to a classical star-tracker, this list is generated by detecting sources in images. Unlike a classical star tracker, however, the sources are detected one-by-one iteratively from raw images reconstructed by an interferometer. This is needed because the signal of the secondary lobes making bright sources shadowing fainter sources as explained in the section 2.2.1. At each iteration, the contribution of the detected source is subtracted from the measured signal. That subtraction requires a precise determination of the position of the source and its brightness. These parameters are retrieved by performing a Gaussian fit as explained in section 2.2.4. The fitting step requires a discrete brightness map whose pixels are smaller than the resolution of the instrument. When in "Lost-In-Space" (LIS) mode, the position of the sources is unknown to the instrument and, thus, the whole sky has to be scanned. It would be inefficient to map the whole sky to spot out a source with a pixel size suited for the Gaussian fit. Therefore, the function proceeds by iterations to refine the region of interest (ROI) as explained in section 2.2.2. The description of this function is represented on Figure 3

2.2.1 Peeling Process

A classical optical star-tracker function only requires three sources to work properly. The nature of these sources is not important as long as they are listed in the onboard catalog and are detectable by the spacecraft. In the case of the RST concept, four

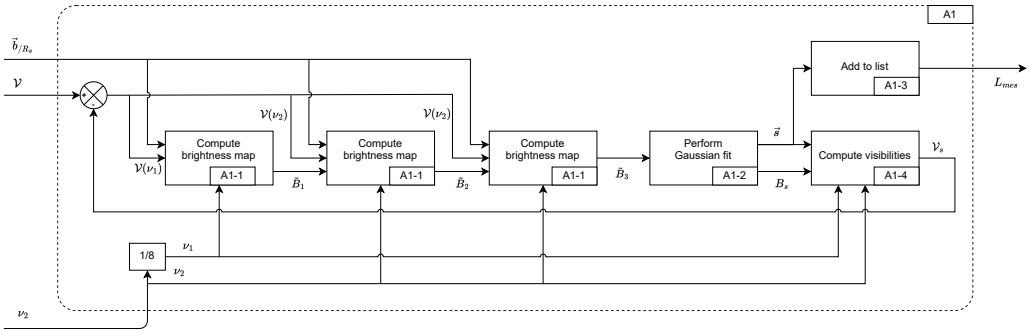

Figure 3: SADT description of the function A1

Sources name	flux (Jy)	size (arcmin)
Cassiopeia A (3C 461)	27104	7.4
Cygnus A (3C 405)	22146	2.3
Taurus A (3C 144, M 1, Crab Nebula)	2008	7.9
Virgo A (3C 274, M 87)	2635	15.0

Table 2: The four brightest sources of the A-team: flux at 50 MHz and angular size, taken from de Gasperin, F. et al. (2020).

sources are requires, in order to determine transform $\mathcal{M}$, which is composed of a rotation and a symmetry.

The low frequency radio sky is dominated by a few bright sources called the *A-team* in addition to the Galactic disk emission that dominates most of the background noise brightness temperature. The fluxes at 50 MHz of the four brightest sources are specified in Table 2. These sources can be expected to dominate the other sources even at very low frequencies, although this assumption has still to be validated since their low frequency spectrum are not really constrained, see (Scaife & Heald, 2012). de Gasperin, F. et al. (2020) propose more accurate modeling of these sources at low frequency with supplementary parameter such as spectral turn-over in addition to the classical power law index deduced for high frequency observations. Thus, it is expected that the main sources that can firstly be detected in the reconstructed map of the sky are amongst the A-team. These sources also have the advantage of being well distributed in the sky. The large angular distance between these sources will improves the accuracy on the transform determination and it will reduces the risk that two of them are missing at same time, e.g., due to possible occultation by the Moon.

Theoretically, four sources are required to fully constraint the transform, but the more sources found, the more accurate the results. As a few very bright sources are expected to dominate the sky, they overshadow the other fainter sources.Indeed, such an interferometer has multiple secondary lobes induced by the geometry of the swarm, whose power are not negligible compare to the main lobe, especially if the baseline configuration show redundancy. If a bright source were to be in the direction of a secondary lobe, its signal could dominate the signal over the contribution of a fainter source in the main lobe, hence hiding it. To address this issue, the function does not look for all the sources in the first reconstructed image but uses an iterative process starting with dominant sources. It performs a "source modeling and subtraction" (also known as "peeling"), similar to what is done by the CLEAN algorithm (Högbom, 1974) in its major cycle. At each it-

eration, the function finds the brightest source, stores its position and brightness, removes its full contribution from the signal, reconstructs a new image and repeats.

The peeling process is a powerful tool, however, in order to perform well, the position and the brightness of the source have to be known precisely. Therefore, the function computes these parameters by fitting a Gaussian around the source. This step requires a brightness map sampling whose pixels are smaller than the resolution of the instrument that is generated as explained in the section 2.2.2.

2.2.2 Brightness Map Reconstruction: Function A1-1

An interferometer can reconstruct a brightness map from interferometric visibilities. The expression of the interferometric visibility (or "visibility" in short) between the nodes i and j is given by:

$$\mathcal{V}_{i,j} = \iint B(\theta_k, \phi_k) \;\; \exp\left(-\iota \, \vec{k} \cdot \vec{b}_{i,j}\right) d\Omega_k \tag{1}$$

where B is the brightness map of the sky, $\vec{b}_{i,j}$ the baseline between the nodes i and j, ι the imaginary unit, $\vec{k}$ the wave vector and $d\Omega_k$ the elementary solid angle in the direction of $\vec{k}$, with spherical coordinates components (θ_k, ϕ_k).

The brightness map can be reconstructed applying a Discrete Fourier Transform (DFT). This map is noted $\tilde{B}$ and is usually called *dirty image*. It is defined as follows:

$$\tilde{B}(\theta, \phi) = \Re\left(\frac{1}{N_{bl}} \sum_{(i,j)} \mathcal{V}_{i,j} \;\; \exp\left(\iota 2\pi \, \nu/c \;\; \vec{s}(\theta, \phi) \cdot \vec{b}_{i,j}\right) \right) \tag{2}$$

This Fourier Transform has a greater computational complexity than the fast Fourier transform (FFT) ($\mathcal{O}(N^2)$ for the DFT compare to $\mathcal{O}(Nln(N)$ for the FFT with N the number of points if N is a power of 2) but can be highly parallelized, which makes its implementation suited for a swarm of satellites with distributed computation capability.

The above Equation 2 specifies how to evaluate the brightness in a given direction. In order to generate a map, the sky is discretized in a pixel array and the brightness of each pixel is computed in the direction of the center of the pixel. The maps used in the simulation are generated using the HEALPix (Hierarchical Equal Area isoLatitude Pixelation) mapping (Gorski et al., 2005; Zonca et al., 2019). This tessellation is suited for full sky imaging as it guarantees that each pixel covers the same surface of the sky. Moreover, the computation of spherical harmonics is made easier thanks to a smart localization and indexation of the pixels. For each pixel of the output map, the brightness is computed using Eq. 2.

2.2.3 Brightness Map Iterations

On the one hand, the whole sky has to be scanned as the position of the sources is completely unknown to the instrument when in *Lost-In-Space* (LIS). On the other hand, the spatial sampling of the map used for the Gaussian fit was taken 10 times smaller than the resolution of the instrument, i.e., $\frac{1}{10}\lambda/D_{max}$. Indeed, a sub-pixel precision can be achieved with such fitting but it requires the source to be at least a few pixels wide. Therefore, the function proceeds by iterations to refine the region of interest (ROI).

The function generates three images using two frequencies to benefit from an increase in resolution as depicted in Figure 4. The frequencies are noted ν_1 and ν_2 and their respective resolution are noted $\Delta\theta_1 = \lambda_1/D_{max} = c/(\nu_1 D_{max})$ and $\Delta\theta_2$. The properties of the images are summarized in Table 3 and listed below:

Name	Image	Freq	size	pixel size	number of pixels
$\tilde{B}_1$	Full sky (Fig. 4a)	ν_1	$4\pi sr$	$\Delta\theta_1/2$	$4\pi(D/8c)^2\nu_2^2$
$\tilde{B}_2$	First *ROI* (Fig. 4b)	ν_2	$5\Delta\theta_1$	$\Delta\theta_2/2$	$\pi(5*8)^2$
$\tilde{B}_{2z}$	Second *ROI* (Fig. 4c)	ν_2	$5\Delta\theta_2$	$\Delta\theta_2/10$	$\pi(5*10)^2$

Table 3: Properties of the images generated during the peeling process

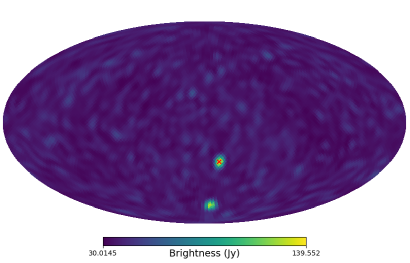

(a) $\tilde{B}_1$ Full sky image at ν_1

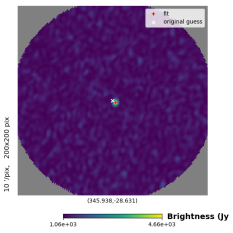

(b) $\tilde{B}_2$ First *ROI* at ν_2

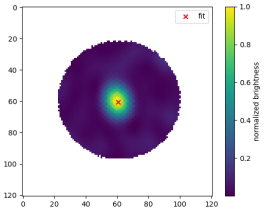

(c) $\tilde{B}_{2z}$ Second *ROI* at ν_2 and the result of the Gaussian fit

Figure 4: Example of the three images generated during an iteration of the peeling process. They were generated during the first iteration of peeling at $\nu_2 = 240$kHz.

- The first image, noted $\tilde{B}_1$, is a full sky image. It is computed at the frequency ν_1 and with a pixel size of $\Delta\theta_1/2$ (see Fig.4a).
- The second image, noted $\tilde{B}_2$, is the first *ROI*. It is generated at frequency ν_2 around the position of the brightest pixel of $\tilde{B}_1$ within a radius of $5\Delta\theta_1$. The pixel size is set to $\Delta\theta_2/2$ (see Fig. 4b).
- The third map, noted $\tilde{B}_{2z}$, is the second *ROI*. It is computed at frequency ν_2 around the brightest point of $\tilde{B}_2$ within a radius of $5\Delta\theta_2$ and with a pixel size of $\Delta\theta_2/10$ (see Fig. 4c).

The angular sizes of $\tilde{B}_2$ and $\tilde{B}_{2z}$ is taken to be 5 times the resolution of the previous image. This factor is a trade-off that is deemed large enough to ensure the source remains in the imaged field and small enough to reduce the computation time. The frequencies used are selected so that $\nu_2 = 8\nu_1$ and $\nu_1 > 30$ kHz. The factor 8 between the two frequencies is chosen to minimize the amount of computation for a given resolution $\Delta\theta_2$. The calculations supporting this result are described in Appendix D. By doing so, it is assumed that the sky brightness remains similar when observing at ν_1 and ν_2. This assumption is discussed in section 3.2. A greater accuracy can be achieved by adding more iterations of refinement along with higher frequencies.

2.2.4 Gaussian Fitting: Function A1-2

A Gaussian fit is performed on the last map $\tilde{B}_3$ using the least squares minimization of the python library *scipy.optimize*. The map dynamical range is resampled between 0 and 1. The Gaussian function fitted is expressed in the following form:

$$G(\vec{s}) = \overline{A} + A \exp\left(\frac{\arccos\left(\vec{s}\cdot\vec{s}_0\right)^2}{2\sigma_0^2}\right) \tag{3}$$

whose parameters $\overline{A}$, A, σ_0, $\vec{s}_0 = (\theta_0, \phi_0)$ are the background brightness, the source brightness, the angular size of the source and its central direction. This Gaussian function assumes that sources have a circular shape. It is not impacted by distortion of the map at very large scale as it uses the angular distance between the considered pixel to the Gaussian center. The position of the fitted source is given by $\vec{s}_0$ and its brightness is retrieved from A after inverting the resampling process.

Nevertheless, the described process does not guarantee to find a true source in the third map. Therefore, rejection criteria are applied in order to exclude bad iterations. The criteria are the following ones:

- The fitting function has converged
- The amplitude of the source is greater than the background fluctuations : $A > 0.5$
- The angular size of the source is similar to the resolution : $\sigma_0 < \Delta\theta_2$
- The fitted function is similar to the original image : $\text{mean}(\|\tilde{B}_3 - G\|) < 10\%$

If all criteria are met, the fit is considered to be successful represented by a success boolean parameter.

2.2.5 Sources Subtraction and Coordinates Storage: Function A1-3 and A1-4

If the Gaussian fit was successful, the position of the found source is stored in a list L_{mes} which is the output of function A1.

Then, its contribution to the signal is estimated by considering it as a point source. The visibilities associated to this source are computed with:

$$\mathcal{V}(s) = B_s \exp\left(-\iota 2\pi\nu/c \;\; \vec{s}_0 \cdot \vec{b}\right) \tag{4}$$

where B_s is the brightness of the source s and $\vec{s}_0$ its direction measured in the *system frame* $\mathcal{R}_s$. This estimation is made possible by considering the satellites to behave as isotropic antennas. Otherwise, the orientation of the satellite would have to be considered whereas their attitude is known in the *absolute frame* $\mathcal{R}_a$ and remain unknown in the *system frame* $\mathcal{R}_s$.

However, the brightness of the source B_s is *a priori* not the same at both frequencies and is only measured at ν_2. The brightness at ν_1 is retrieved from the Equation 2 in the same direction $\vec{s}_0$ with the visibilities at ν_1. These visibilities are then subtracted to the total visibilities $\mathcal{V}_{n+1} = \mathcal{V}_n - \mathcal{V}(s)$. Thus, the contributions in the secondary lobes of the source are removed. This cleaning step enables to find more sources and allows to have a better estimation on the position of the sources found afterward.

This process is iterated. In order to exclude spurious detection of residuals in the close vicinity of removed sources, a mask is applied to the reconstructed map. The brightest sources are expected to have a large angular separation like the A-team sources. Selecting a large mask radius speeds up the process. For our application, the masks are centered on $\vec{s}_0$ with a radius of 5°. In case the gaussian fit is unsuccessful, the function performs a visibility subtraction anyway and masks out the region, using the position and amplitude of the maximum pixel in third map $\hat{B}_3$. The process is iterated until 5 consecutive fits are unsuccessful. A maximum number of iterations N_{it} is also set to prevent the function from running for too long. This parameter was set to $N_{it} = 10$.

Following these steps, a list of sources position is retrieved. This list is noted L_{mes} as depicted in Figure 2. It is the output of the box function A1.

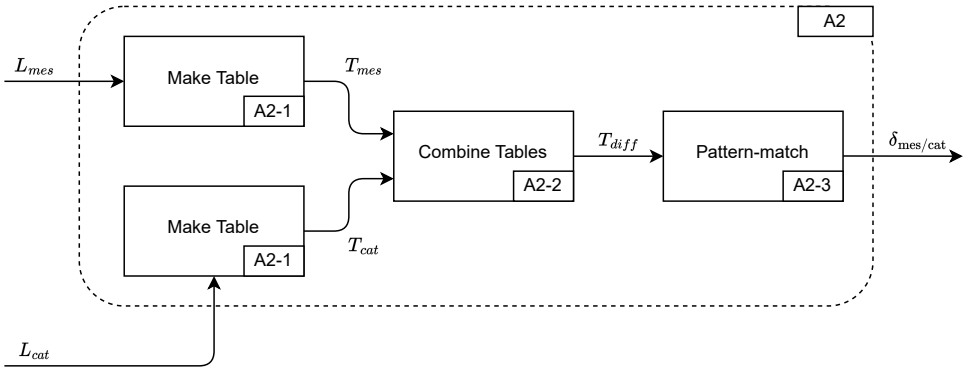

Figure 5: SADT description of the function A2

2.3 Pattern Matching: Function A2

Once the sources positions are listed, they are compared to the catalog. The method is the same as the one used for a classical star-tracker and is called pattern matching. It uses the geometrical properties of the patterns formed by the sources as they are independent of the direction on the sky. It is also independent of the brightness of the sources which is a parameter that is unreliable for this application. The description of this function is represented on Figure 5

2.3.1 Geometric Properties Table: Function A2-1

Two tables of the geometric properties of the sources are built on-board for the list of measured sources L_{mes} and the catalog sources L_{cat}. The tables entries are composed of three parameters (a, b, γ) derived from the ones used by Liebe (1995). For each source and for every spherical triangle of three sources that can be composed with it, the table entries are the angular distances a and b between this source and the two others as well as the bi-angle γ between these two as seen from the source. These geometrical parameters are described in Figure 6. Although, some pattern matching algorithms only use the distances between the stars or only use the nearby stars (Kolomenkin et al., 2008; Kim & Bang, 2020), it is not applicable in this case. Indeed, the sources that can be recognized are spread all across the sky and are in small number which forces to use geometrical parameters that are valid over the sphere. The entry γ makes the match more reliable.

The bi-angle is calculated using the following formula:

$$\cos(\gamma) = \frac{\cos(c) - \cos(a)\cos(b)}{\sin(a)\sin(b)} \tag{5}$$

With these parameters, the table entries are different for the same triangle depending on the source considered, so that 3 entry lines are generated for each triangle. Using every possible triangles may lead to very long table. For instance, if Ns_{mes} sources were found, its table L_{mes} has dimensions of $Ns_{\mathrm{mes}}.(Ns_{\mathrm{mes}}-1).(Ns_{\mathrm{mes}}-2)/2 \times 3$. However, only three sources are sufficient to compute a rotation matrix. As the subtraction process is not perfect the number of measured sources is limited and Ns_{mes} is expected to vary from 4 to 20. Also, the catalog table is computed for the brightest sources with a number of source twice greater $2\times Ns_{\mathrm{mes}}$, with a minimum of 10. This results in tables of 10^3 records reasonable for on-board computing.

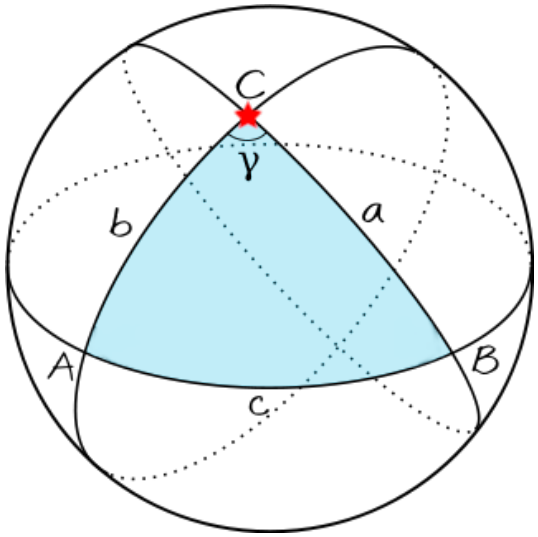

Figure 6: The parameters (a, b, γ) used to characterized the source C in a triangle ABC of three sources.

2.3.2 Table Difference: Function A2-2

In order to spot out a matching pair of triangles, their entries in their respective table are compared. A matching pair share similar entries. The difference between L_{mes} and L_{cat} is computed by generating a three dimension table T_{diff} whose first dimension refers to the index of the triangles in L_{mes}, second dimension refers to the index of the triangles in L_{cat} and last dimension the difference of geometrical properties (Δa, Δb and $\Delta\gamma$). An example of this table is depicted on Fig. 7a.

2.3.3 Voting Scheme: Function A2-3

The pattern matching algorithm requires a good tolerance to false positive (FP). Indeed, during the previous step of the *RST* algorithm, various sources not listed in the catalog can be found. For instance, Jupiter radio emissions (Zarka, 2004) may appear as bright spots on the reconstructed images, as well as artifacts of the reconstruction may be interpreted as a source. The algorithm has to be able to reject such FP. The other way around, the table made from the catalog contains more sources than the list of detected sources. A bright source of the catalog may not be found if, for instance, one is hidden by the Moon or the Sun. Thus, the matching has to be performed only with the sources of interest.

For that purpose, a voting system is implemented, similar to what was used by Kolomenkin et al. (2008). For each matching pair of triangles, the associated pair of sources — one measured, one from the catalog — receives a vote. A pair of triangles is said to be matching if the difference between their parameters are smaller than a set of thresholds. The chosen thresholds suppose that the sources are found within a radius equal to the angular resolution $\Delta\theta_2$ around their known position. For a and b, the threshold is twice the resolution:

$$\|a_{\text{cat}} - a_{\text{mes}}\| \leq 2\Delta\theta_2 \tag{6}$$

For γ, the threshold is:

$$\|\gamma_{\text{cat}} - \gamma_{\text{mes}}\| \leq 2\Delta\theta_2\left(\frac{1}{a_{\text{cat}}} + \frac{1}{b_{\text{cat}}}\right) \tag{7}$$

The latter formula is a simplification considering $\Delta\theta_2 \ll a$, which is verified here. Indeed, the detected sources are separated by a distance of at least the radius of the mask applied during the peeling process. Thus, $a, b > 5° \gg \Delta\theta_2$.

Counting the votes generates a table V of dimensions Ns_{mes} by Ns_{cat} representing the number of votes per pair of sources (see Fig. 7b). Each detected sources is associated to the source from the catalog that shares the most votes. Furthermore, in order to reject FP, a threshold on the number of vote is applied. The threshold used is given by:

$$\max\{\ 3,\ \text{mean}(V) + 3 \times \text{std}(V)\ \} \tag{8}$$

Only the sources that received a number of vote significantly higher than the others are selected. A minimum of three is set to reject bad runs. If only three true sources are found, each sources should receive three votes. If less than three matches are found, the computation of the swarm attitude is considered to have failed and has to be run again with new measurements.

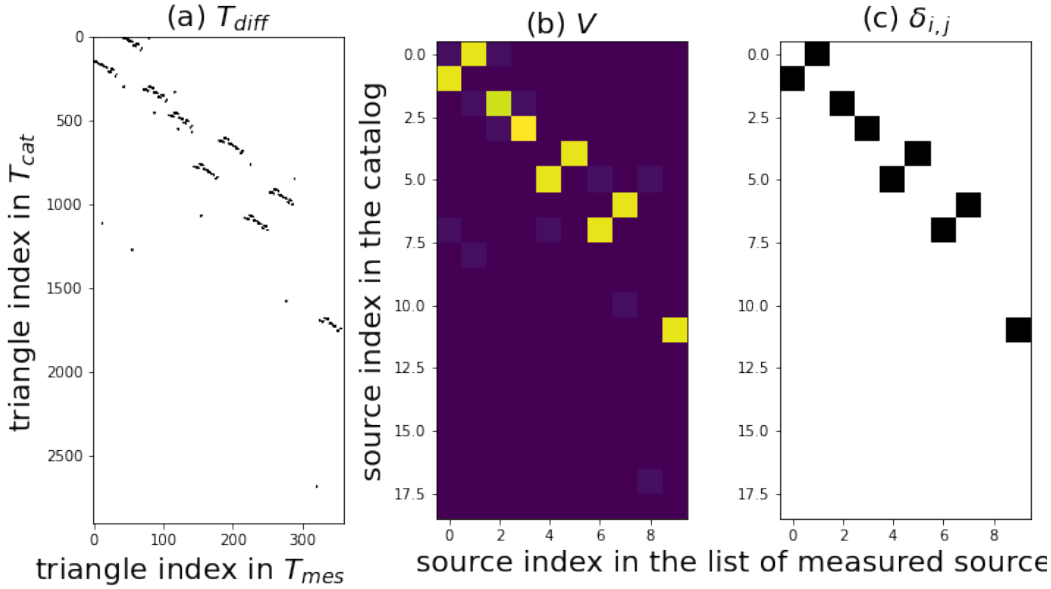

Figure 7: Example of tables generated for the voting method. a) L_{diff}, b) V, c) P_π

Applying this threshold generates a permutation table P_π that tells if the indices i in the list of found sources L_{mes} correspond to the same source as the indices j in the catalog L_{cat} (see Fig. 7c). This identification is necessary to compute the transform that links the two sets.

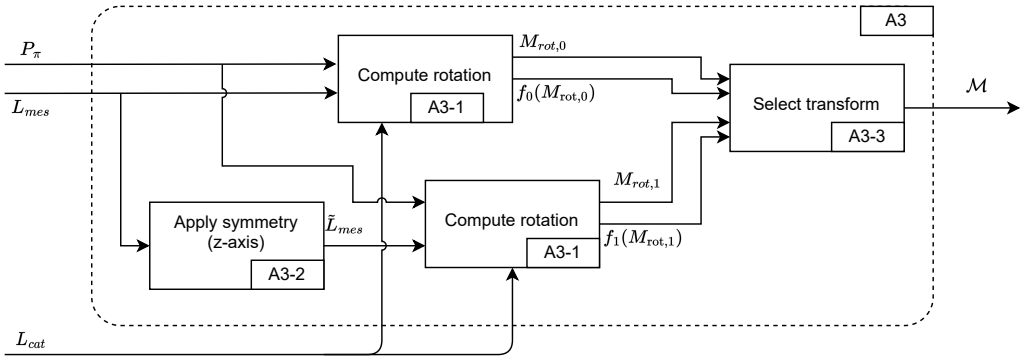

Figure 8: SADT description of the function A3

2.4 Transform Computation: Function A3

Once the identification between the detected sources and the catalog is made, their positions can be compared. The algorithm computes the best transform that links the two sets of position.

That transform may include a reflection which is then called an "improper" rotation. The presence of a reflection is represented by a Boolean noted $\nVdash_r$ that is true (= 1) if the transform includes a reflection. The transform $\boldsymbol{\mathcal{M}}$ can be expressed as the product of a pure rotation matrix $\boldsymbol{M}_{\mathrm{rot}}$ and a potential reflection matrix $\boldsymbol{M}_{\mathrm{ref}}(\nVdash_r)$ as $\boldsymbol{\mathcal{M}} = \boldsymbol{M}_{\mathrm{rot}} \cdot \boldsymbol{M}_{\mathrm{ref}}$

$$\boldsymbol{M}_{\mathrm{ref}}(\nVdash_r) = \begin{cases} \boldsymbol{I}_3 & \text{if } \nVdash_r = 0 \\ \boldsymbol{M}_{\parallel z} = \begin{pmatrix} 1 & 0 & 0 \\ 0 & 1 & 0 \\ 0 & 0 & -1 \end{pmatrix} & \text{if } \nVdash_r = 1 \end{cases} \tag{9}$$

The reflection is chosen to be along the z-axis. The choice of the axis of reflection is not important as every reflection is equal to another reflection up to one rotation (see Appendix F). Hence, by applying any given reflection to the coordinates of L_{mes}, the computation of the reflection comes down to optimizing the rotation that links these new coordinates to the ones of the catalog.

The presence of a reflection is not a linear parameter and thus cannot be optimized using regular optimization scheme. Instead, the rotation matrix $\boldsymbol{M}_{\mathrm{rot}}$ is optimized for both states of the reflection matrix $\boldsymbol{M}_{\mathrm{ref}}$, i.e. with and without a reflection.

The optimization of the rotation matrix is performed by minimizing the function $f(\boldsymbol{M}_{\mathrm{rot}})$ defined by Eq 10. It is the quadratic sum of position differences weighted by the brightness of the sources:

$$f_{\nVdash_r}(\boldsymbol{M}_{\mathrm{rot}}) = \sum_i B_i \arccos\left(\vec{s}_{\mathrm{cat},i} \cdot (\boldsymbol{M}_{\mathrm{rot}} \boldsymbol{M}_{\mathrm{ref}}(\nVdash_r) \cdot \vec{s}_{\mathrm{mes},i})\right)^2 \tag{10}$$

The minimization of f corresponds to the sub-function A3-1 in the SADT diagram of the function (see Fig. 8). It is computed once with the original coordinates (i.e., with $\boldsymbol{M}_{\mathrm{ref}} = \boldsymbol{I}_3$) and once with the reflected coordinates (i.e., with $\boldsymbol{M}_{\mathrm{ref}} = \boldsymbol{M}_{\parallel z}$). The coordinates are reflected through the sub-function A3-2.

The output transform is the one that has the best fit. Let $\boldsymbol{M}_{\mathrm{rot},\,0}$ be the optimized rotation matrix for a pure rotation transform and $\boldsymbol{M}_{\mathrm{rot},\,1}$ be the optimized rotation ma-

trix for a transform with a reflection of axis z. If $f_0(\boldsymbol{M}_{\text{rot, }0}) < f_1(\boldsymbol{M}_{\text{rot, }1})$, then the return transform is $\boldsymbol{\mathcal{M}} = \boldsymbol{M}_{\text{rot, }0}$. Otherwise, the return transform is $\boldsymbol{\mathcal{M}} = \boldsymbol{M}_{\text{rot, }1}\boldsymbol{M}_{\|z}$. This last step is represented by the sub-function A3-3.

3 Methods of Simulation Study

The efficiency of the *RST* algorithm is evaluated through a simulation pipeline. Its accuracy is computed over multiple runs of the pipeline with the objective of studying its sensitivity to various parameters, namely: the frequency, the noise level and the swarm topology. The inputs for the algorithm are generated with a simulation environment and the outputs are evaluated with metrics. The following subsections successively describe how the models of the simulation environment are used to generate the inputs as well as the evaluation metrics.

3.1 Interferometer Modeling

The satellites are randomly placed inside a sphere of 100 km of diameter with an uniform distribution. The same geometry was used in a simulation of the swarm of NOIRE (Cecconi et al., 2018). The baselines are computed from these positions. In order to model the unknown rotation of the frame in which those baselines are expressed, a random rotation is applied to the map of the sky and the point sources. This rotation is referred to as $\boldsymbol{\mathcal{M}}_{\text{simu}}$ in reference to Section 2.4.

3.2 Signal Modeling

The *RST* algorithm is meant to work at very low frequency, below 1 MHz. However, as mentioned previously, the sky remains mostly unknown in this spectral range. Novaco and Brown derived rough contour maps of the Galaxy using data from RAE 2 (Novaco & Brown, 1978) down to 1.31 MHz. These data enables to constraints the average brightness of the models but cannot be used to generate a source catalog. On the other hand, measurements performed with SunRISE (Kasper et al., 2021) could be used to confirm the detection level of a few bright sources. The commissioning phase of NOIRE will include a rough mapping of the sky enabling to calibrate the source catalog to be used for the *RST* function. For the sake of the simulation, the low frequency sky is approximated with a model derived from observations at higher frequency.

The signal of interest for this algorithm is the correlation product measured between each pair of nodes. The simulation directly estimates the visibilities based on a sky model and a noise model. From Eq. 1, the visibility is presented as a sum of contributions from all sources and directions. Thus, each contribution can also be computed independently. The noise is supposed to be uncorrelated so that it can be computed independently too. Its contribution in the visibilities is notes ξ. The sky model implemented is separated into two categories: diffuse emission and point sources whose contribution to the visibilities are respectively noted $\mathcal{V}_d$ and $\mathcal{V}_{\text{ps}}$.

The total visibilities $\mathcal{V}$ can be expressed as $\mathcal{V} = \mathcal{V}_{ps} + \mathcal{V}_d + \xi$. The following subsections describes how each of these components are modeled.

The sky model implemented does not take into account foreground sources and transient emissions. For instance, the solar radio bursts, the man-made Radio Frequency Interferences (RFI), the Earth Auroral Kilometric Radiation (AKR) or other planetary emissions are not included in the sky model. Nonetheless, these emissions appear brighter than most sources when observed at the Moon and are not negligible (Zarka et al., 2012). Transient sources are not considered as the swarm is expected to have moments when their perturbations are negligible. Foreground sources, on the other hand, can be partially shielded by the Moon. In order to study the *RST* function performances while re-

ceiving signal from such sources would require to implement specific models for each of them and, thus, be part of a deeper study.

3.2.1 Point Source Model

For the unresolved sources, the visibilities are defined as a sum over the point sources as:

$$\mathcal{V}_{ps\ (i,j)} = \sum_s B_s \exp\left(-\iota\ \vec{k}_s \cdot \vec{b}_{i,j}\right) \tag{11}$$

This modeling supposes that the sources not resolved by the instrument behave like point sources. This assumption is highly debatable as low frequency emissions undergo a lot of scattering (Jester & Falcke, 2009). The apparent angular size of these sources may be much large depending on the observation frequency making this modeling untrustworthy. Let us remind the *RST* algorithm can also be used at higher frequency were this effect is no longer troublesome.

This signal is modeled using a list of objects considered as point sources gathered from the LOFAR database[1]. at 60 MHz. More than 200 sources are taken from this database.

Nevertheless, the brightness of the sources at very low frequency cannot be expected to be the same at very low frequency and or 60 MHz. In particular, the low frequency emissions are expected to be impacted by the synchrotron self-absorption. This effect is noticeable over the low frequency spectrum of the Galaxy where a spectral turnover is observed around 2 MHz (Jester & Falcke, 2009). Other low frequency sources are showing a similar turnover (Vinyaikin et al., 1987; McKean et al., 2016; Arias et al., 2018; Stanislavsky et al., 2022). It was chosen to modeled the low frequency spectrum of all sources to behave as the spectrum of the Galaxy. This spectrum was approximated by (Jester & Falcke, 2009) with two power laws. With this approximation, the brightness temperature of the sources for $\nu < 2$ MHz, can be estimated with:

$$T(\nu) = T(60\text{MHz}) \left(\frac{60\text{MHz}}{2\text{MHz}}\right)^{-2.53} \left(\frac{\nu}{2\text{MHz}}\right)^{-0.3} \tag{12}$$

It would be more realistic to use different models for sources close to, or far from, the Galactic plane or to have a different treatment for extra-galactic sources. Yet, the low frequency sky remains unknown and a change of model would not be significantly more realistic. Moreover, it does not change the way the algorithm process.

3.2.2 Diffuse Emission Model

The diffuse emission is spatially sampled over small sections of solid angle $\Delta\Omega$ as:

$$\mathcal{V}_{d\ (i,j)} = \sum_{\vec{k}} B(\Omega_k)\ .\ \exp\left(-\iota\ \vec{k} \cdot \vec{b}_{i,j}\right)\ \Delta\Omega \tag{13}$$

This Equation is valid if the sampling step is small enough so that the integrated term in Eq. 1 can be considered constant. This correspond to solid angles smaller than the angular resolution; i.e. $\Delta\Omega \ll (\lambda/D_{max})^2$. The pixel size chosen to compute the continuum is set at least 4 times smaller than the angular resolution.

At high angular resolution, the spatial sampling step required may be significantly smaller than the scale of the element of the diffuse sky. Besides, with a small spatial sam-

[1] `https://lcs165.lofar.eu/`

pling, the method described above can be computationally heavy. When in this situation, another method is implemented. It uses the Spherical Wave Harmonic Transform (SWHT) which was developed by Carozzi Carozzi (2015). More details on that method can be found in Appendix C.

This signal is modeled using a Global Sky Model (GSM) map of the sky at 50 MHz (de Oliveira-Costa et al., 2008) is used as reference as it is the lowest frequency map that is almost complete. This map can be obtained in HEALPix format using the python interface `pyGDSM`[2] with an angular resolution scaling down to 7 arcmin which is smaller than the angular resolution that can be achieved by NOIRE at 1 MHz.

As mentioned, the point sources are modeled separately from the continuum whereas the GSM map already contains the signal coming from these sources. Plus, their signal is convolved with the impulse response of the instruments used for this survey. In order to adapt the model to our needs, the following steps are performed; for each point sources selected in the catalog, a disc of radius $r_1 = 1.5°$ centered on the source position is uniformly set to a constant value. This value is the median brightness computed in the ring centered on the source and with inner and outer radii r_1 and $1.25\, r_1$. The radius is set to 1.5° in order to be larger than the widest point spread function (PSF) of the instrument used to generate this map.

3.2.3 Noise Model

The modeling of the visibilities mentioned above does not include any form of noise. Still, noise can be introduced in the measurements at various steps. A noise term ξ is added in the simulation as described by Thompson et al. (2017). The RMS noise on the real part of a visibility for a given baseline can be expressed as:

$$\sigma_n = \frac{S_{\text{sys}}}{\sqrt{2\tau\Delta\nu}} \tag{14}$$

where $\Delta\nu$ is the acquisition bandwidth and τ is the integration time.Their product is named the integration factor. S_{sys} is the system equivalent flux density (SEFD) and can be expressed as a function of the system temperature T_{sys} as follows:

$$S_{\text{sys}} = \frac{k_B T_{\text{sys}}}{\eta A_{\text{eff}}} \tag{15}$$

where k_B is the Boltzmann constant, A_{eff} is the effective area of the antenna, η is the system efficiency. For an ideal isotropic antenna, one has $\eta A_{\text{eff}} = \lambda^2/4\pi$.

At very low frequency, the system temperature is dominated by the sky temperature defined by:

$$\begin{aligned} T_{\text{sys}} = T_{\text{sky}} &= \frac{1}{4\pi}\iint T_B(\theta,\phi)G(\theta,\phi)d\Omega \\ &= \frac{1}{4\pi}\Big(\iint T_{\text{diff}}(\theta,\phi)d\Omega + \sum_s T_s\Big) \end{aligned} \tag{16}$$

where $G(\theta,\phi) = 1$ is the antenna gain and T_B is the sky brightness temperature. In this modeling, it comes down to summing up the average temperature of the diffuse sky T_{diff} and the brightness temperature of the point sources T_s.

With that, the noise is a function of the integration factor $\tau\Delta\nu$. We define an dimensional factor α reprensenting the noise level defined as:

$$\alpha = \frac{1}{\sqrt{2\tau\Delta\nu}} \tag{17}$$

[2] `https://github.com/telegraphic/pygdsm`

Thus, the RMS noise on the real part of a visibility can be rewrite as $\sigma_n = \alpha S_{\text{sys}}$. Finally, the noise $\xi_{i,j}$ is randomly drawn following:

$\|\xi_{i,j}\| \hookrightarrow \mathcal{N}(\sqrt{2}\sigma_n, 0)$

Arg $\xi_{i,j} \hookrightarrow \mathcal{U}([-\pi, \pi[)$

3.3 Evaluation of the Accuracy

The output of the *RST* is a transform that includes a rotation. Its purpose is to provide directional information. The accuracy of the function is evaluated as the maximum angular separation between directions transformed by the simulated transform and the transform returned by the *RST* function. The directional error ϵ is expressed as:

$$\epsilon = \max_{\vec{s}} \quad \arccos\left((\boldsymbol{\mathcal{M}}_{\text{mes}} \cdot \vec{s}) \cdot (\boldsymbol{\mathcal{M}}_{\text{simu}} \cdot \vec{s})\right) \tag{18}$$

The vectors $\vec{s}$ that maximize the angular separation are the vectors parallel to $\vec{m}$ the rotation axis of ${\boldsymbol{\mathcal{M}}_{\text{mes}}}^T \boldsymbol{\mathcal{M}}_{\text{simu}}$ as explained by (Huynh, 2009). These vectors can be defined as part of the set $\mathcal{S}$ expressed as:

$$\mathcal{S} = \left\{\vec{s} \in \mathbb{R}^3 \quad | \quad \vec{s} \cdot \vec{m} = 0 \quad \text{and} \quad \|s\| = 1\right\} \tag{19}$$

The vector $\hat{\vec{s}}$ used for the estimation of the error is computed as the cross product of $\vec{e}_x = (1, 0, 0)$ with $\vec{m}$. So that, $\hat{\vec{s}} = \vec{m} \wedge \vec{e}_x / \|\vec{m} \wedge \vec{e}_x\|$.

4 Results

The performances of such an algorithm are difficult to assess as its output accuracy varies significantly with multiple parameters. It was chosen to study a few features of the algorithm looking at its stability and sensitivity to a few parameters. Yet, the study was designed to observe the sensitivity of features related to star-tracker performances.

There is no agreed standard for measuring star-tracker performance, however (Kolomenkin et al., 2008) defined a set of features to characterize a star-tracker function. A few of these features could apply as well to the *RST* as presented in this section:

- Accuracy: Directional error
- Source identification rate
- False star Tolerance
- Speed and memory performances

4.1 Accuracy

The accuracy of the directional information induced by the accuracy of the rotation matrix is estimated using the Equation 18. This accuracy is computed at three different frequencies $\nu_2 = \{240, 400, 800\}$ kHz. The number of iterations for the peeling is set to $N_{it} = 10$ for every simulation presented here.

When the noise amplitude is negligible, the accuracy of the method is associated to the resolution of the instrument in the direction of the sources of interest. Thus, it is function of the frequency and the topology of the swarm. The topology of the swarm is a parameter that is constrained by the scientific objectives of the mission therefore the *RST* function should accommodate to it. The evaluation of the swarm topology to be performed requires a study on its own and is not addressed in this study. The swarm configurations were randomly generated as described in section 3.1. When the noise amplitude is dominant, the topology of the swarm has a reduced impact and the frequency has a more predominant influence.

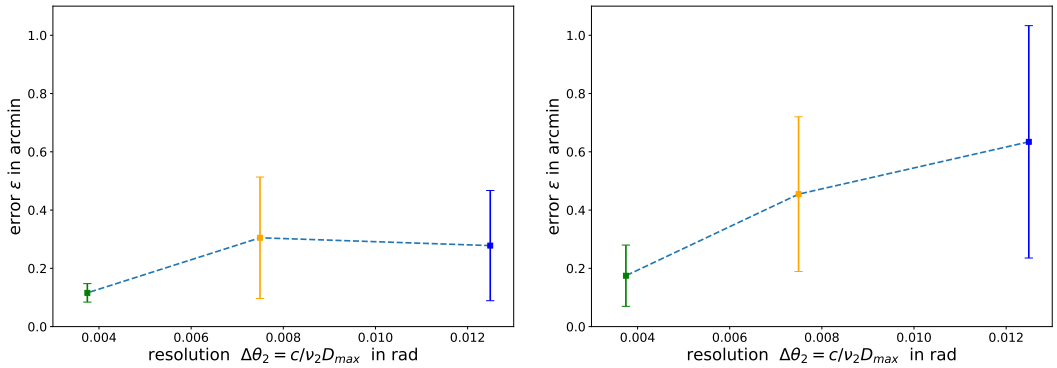

(a) without addition of noise $\alpha = 0$

(b) with dominant noise $\alpha = 0.03$

Figure 9: Directional error ϵ in arcmin as a function of the resolution $\Delta\theta_2 = c/(\nu_2 D_{\max})$. The values are averaged over 10 random configurations and the error bars represent the standard deviation computed among the configurations. The values are computed for two level of noise: (a) $\alpha = 0$, (b) $\alpha = 0.03$. In figure (b), the error of a single configuration is averaged over 10 random noise draws. Then the standard deviations are computed among the different configurations.

The observation frequency defines the maximal instrument resolution for a given size $D_{\max}$ as $\Delta\theta_2 = c/(\nu_2 D_{\max})$. The sensitivity of the accuracy ϵ to the observation frequency ν_2 is plotted as a function of the resolution $\Delta\theta_2$ on Figure 9. On these plots, the accuracy is averaged over a set of 10 random configurations of the interferometer. The same 10 configurations are used for each value of $\Delta\theta_2$. The error bars represent the standard deviation computed among the configurations at each frequency. They highlight the variations that can be observed between various configurations for the same frequency. This plot was generated twice, with and without addition of noise. On the graph 9a no noise were added and on the graph 9b, the noise level was set to $\alpha = 0.03$ as the noise level is expected to be dominated as explained thereafter. According to the plot with noise, it seems that the accuracy is proportional to the instrument resolution. As well, the error range enlarges as the frequency decreases. It suggests, as expected, that increasing the resolution increases the accuracy. However, this trend is less visible when looking at the plot without noise. In this case, the topology of the swarm appears to have a somewhat similar influence on the accuracy as the frequency. The sensitivity of the instrument to the swarm topology would requires a dedicated study.

The robustness of the method with regard to noise is a major concern at very low frequencies. Indeed, for such an instrument, the noise is expected to be dominated by the sky, thus the noise amplitude is driven by the acquisition parameters as detailed in section 3.2.3. With too much noise, the interferometer is not able to identify sources from the diffuse emission making the *RST* function inefficient. The sensitivity of the method in regards to noise is studied by computing the accuracy as a function of the noise level α as represented on Figure 10. The sensitivity is evaluated for the 3 frequencies ν_2. Also, the accuracy computed without noise are represented with dotted lines. As the choice of the configuration can have a significant impact, all the accuracy point of this plot are computed with a single representative configuration. Also, for a given noise level, significant variations can be observed between different noise draw. This effect is alleviated by averaging each accuracy value over 10 random noise draws for each noise level. These variations are represented by the envelopes which vertical range are plotted using the standard deviation of accuracy computed among the 10 draws.

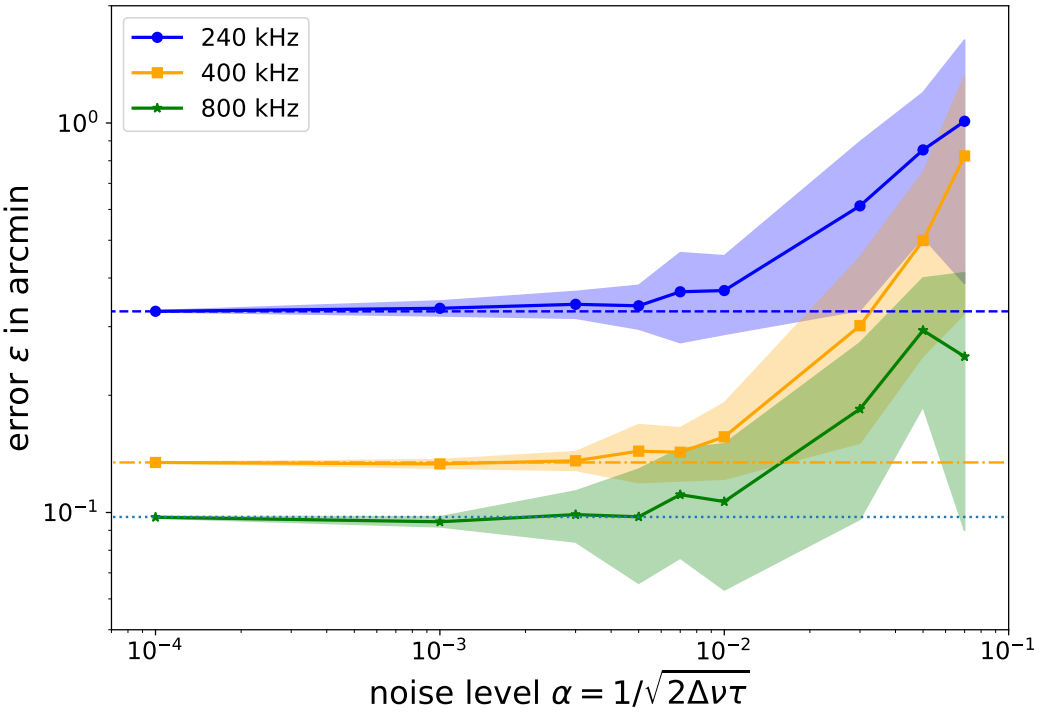

Figure 10: Directional error ϵ in arcmin as a function of the noise level α for 3 pairs of frequencies. The directional errors when no noise is added are displayed with dotted lines.The envelopes highlight the standard deviation observed among the random draws for each noise level.

Figure 10 highlights that noise has a negligible impact for values of noise level $\alpha < 3.10^{-3}$. In this range, the accuracy is mainly driven by the swarm configuration for a given frequency. As expected, when the noise level increases, the accuracy deteriorates. When generating this plot with different configurations, the curves start matching above $\alpha > 10^{-2}$. It suggests that in this range, the errors are dominated by the noise and the configuration has a negligible contribution. For noise level above $\alpha > 0.1$, only a few runs were able to provide a transform matrix. The other runs were unsuccessful because they detected less than 3 sources among the 10 iterations. This can be explained by the multiplication of noise-induced artifacts in the reconstructed images. As the sources are surrounded by artifacts the Gaussian fitting is less consistent and most sources are invalidated by the rejection criteria. This leads to a lower limit for the integration factor: $\tau\Delta\nu > 50$. For example, it corresponds to a frequency band of 1 kHz and an acquisition time of 50 ms. In comparison, the strongest requirement on the integration factor from the sciences objectives is $\tau\Delta\nu = 10^3$. Also, in this operating range of the algorithm, the retrieved transform matrix does not induce error higher than 1 arcmin at each frequency. It makes us confident about the ability of the *RST* method to achieve accuracy better than 1 arcmin consistently. As the trends observed at noise level above $\alpha > 10^{-2}$ appear to be independent on the configuration draw, the aforementioned results are expected to be general to the method.

4.2 Source identification rate and false star tolerance

The number of identified sources is key as at least 3 sources are needed to compute the transform matrix. All simulations presented here were run with 10 iterations of peel-

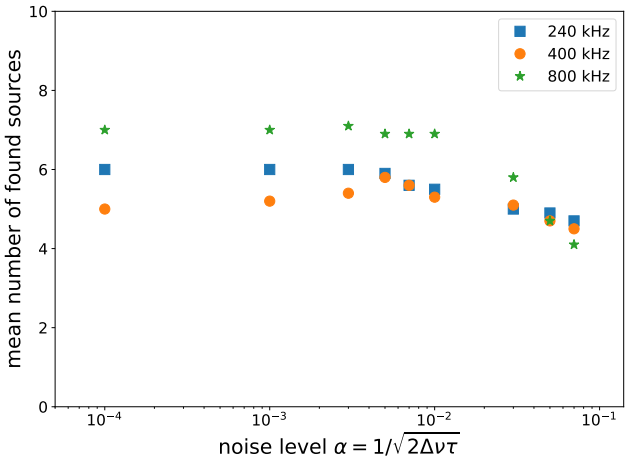

Figure 11: Mean number of true sources found in 10 iterations of peeling for all simulations

ing leading to a maximum number of found sources of 10. In practice, several iterations are rejected. Either it zooms in places were no sources can be found — in the Galactic background or in a noisy spot — or the image around the source is too noisy to pass the rejection criteria.

Among the found sources, only a small amount are false positive (FP). No more than two FP per simulation are observed throughout all the simulations. It means that the rejection criteria are efficient at selecting the sources.

On the other hand, the pattern matching function appears to be robust to FP. No simulations have seen the pattern matching function failing at rejecting a FP even when manually adding extra sources. Still, the function is not able to perform if too many FP remain as the minimum number of vote assumes that half the sources are true positives. Thus, the rejection criteria for FP could be softened in order to allow more source detections and potentially a better precision.

Figure 11 shows that the efficiency of the sources detection remains consistent for noise level under $\alpha < 3.10^{-2}$ and undergoes severe deterioration for higher noise level. With this in mind, the recommended range of use for the *RST* function is for $\alpha < 3.10^{-2}$ which is approximately $\tau\Delta\nu > 500$. For example, it corresponds to a frequency band of 10 kHz and an acquisition time of 50 ms. Again, the strongest requirement on the integration factor from the sciences objectives is $\tau\Delta\nu = 10^3$ for comparison.

4.3 Memory and Speed Performances

The speed performance of the *RST* function may be critical for *Lost-In-Space* (LIS) mode. Indeed, once the LIS algorithm has computed a rotation transform, the *Tracking* mode is engaged. This function is similar to the LIS function except that rather than imaging the whole sky, it directly reconstructs images in the direction of the identified sources. For that, the new position of the sources is estimated using the knowledge of their previous position.

Thus, if the LIS process is too slow, the transform matrix would have changed too much before engaging the tracking mode so that the prediction on the sources position is too inaccurate for the algorithm to work. Therefore, the run speed of the *RST* func-

tion is constrained by a maximum delay. This delay depends on the speed of changes of the transform matrix which is highly dependent on the method recovering the swarm topology. The design of this method could have a major impact on the delay that can be acceptable between the two modes.

The time needed between the acquisition and the knowledge of the transform matrix can be separated into two steps. During the first step, the visibilities have to be computed and gathered to a computing node. For this step, the measured signals have to be broadcasted among the swarm while computing their correlation coefficients. The time taken by this step depends on the communication strategy and data rate inside the swarm which is beyond the scope of this study. The second step consists in running the *RST* algorithm presented here on a satellite.

The algorithm has to be run on a single satellite as it cannot be parallelized and cannot take advantage of the swarm to distribute the computation. It directly affects the run speed of the *RST* algorithm. The peeling technique is intrinsically iterative and cannot be parallelized. Moreover, for each iteration, the zooming method described here generates three images that have to be computed one after the other. Which means this cannot be parallelized either. Some implementations of the CLEAN algorithm suggest that in some cases it is possible to peel a few sources in a single iteration which could speed up the process (Steer et al., 1984; Cornwell, 2008).

A priori, the computation time is dominated by the image reconstructions and the other steps can be neglected. The computation complexity of the image reconstructions can be expressed as proportional to $N_{it} \cdot \nu_2^2$. This computational complexity highlights that this technique does not adapt well to higher frequency. Still, this is a two-frequency zooming and more steps can be added to adapt better to higher resolution requirements. Also, the complexity suggests that the number of peeling iterations should not be increased too much for the sake of run speed. This qualitative estimation is given as the computation time achieve on a personal laptop is not representative of what can be achieved on-board. Yet, Figure 12 highlights the trend of the computation time as a function of the frequency ν_2. A quadratic variation seems to appear. The computation were done on a laptop with a RAM of 32 GB and a processor Intel CORE i7. However, the run time highly depends on the memory allocation at the moment of the run which is greatly impacted by the usage of various softwares at the same time.

5 Discussion About the Limitations

The results presented in this study are conditioned by the environment of simulation, that has some limitations.

The sky is modeled as described in Section 3.2. For now, no elements can tell if this modeling is far from the truth or not. For instance, if the ratio of brightness between the point sources and the Galactic background were to be significantly different, the result would be greatly impacted and this method might become irrelevant. Further measurements are therefore needed at very low frequencies with current facilities, like LOFAR (van Haarlem et al., 2013), NenuFAR (Zarka et al., 2012), or space demonstrator, to assess and constraint the overall spectral behavior.

Also, at very low frequency, the radio signal is supposed to be significantly scattered along the line of sight by the interstellar medium (ISM), especially for signal coming from sources close to the Galactic plane (Oberoi & Pinçon, 2003). The angular scattering broadens the apparent size of point sources. This effect cumulates with the lack of angular resolution at lower frequencies. These effects have important consequences. Firstly, it is harder to distinguish sources from the diffuse emission. Secondly, it makes the Gaussian fitting less reliable. And thirdly, the sources subtraction may leave signif-

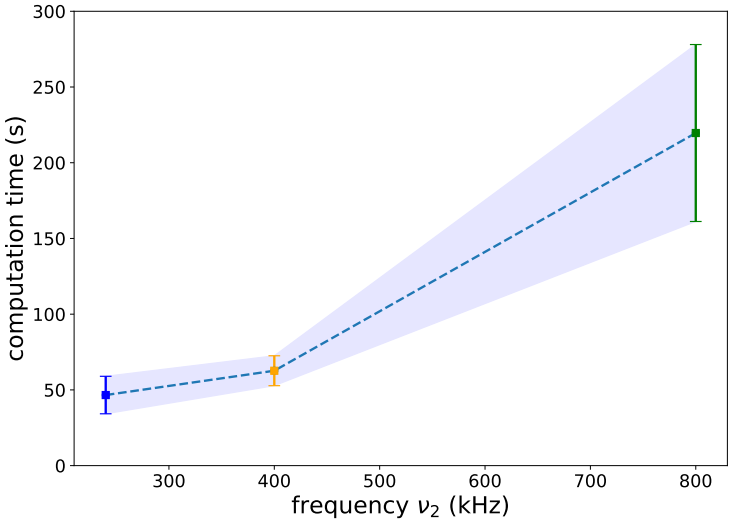

Figure 12: Computation time as a function of the frequency. The runs considered are the ones that does not add noise and generally find the most sources. The number of iterations remains set to 10. The error bars represent the standard deviation observed among the 10 configurations. However this variation is mostly explained by the memory usage of the laptop at the moment of the run.

icant residuals. All these consequences limits the operating range of the *RST* function and requires a deeper study.

Similarly, emissions coming from large bright sources like the Earth and the Sun also appear as large bright spots that could dominate a large fraction of the sky. They present the same issues, especially concerning the remaining residuals after the sources subtraction. Yet, they can be mitigated by using better models.

Furthermore, the simulation of the noise remains simple and cannot represent the whole complexity of the errors that can be introduced in the visibilities and the images. For example, errors on the clocks synchronization, on the topology of the swarm or on the antennas calibration, all lead to errors that cannot be represented only by the complex term ξ added to the visibilities. The form and amplitude of these noises depend on multiple elements like the synchronization algorithm or the relative motion of the satellites. These features are yet to be studied and the noise they induced is unknown for now. These noises are expected to be negligible compared to noise induced by the antenna temperature. If not, the operating range of the algorithm might be impacted.

On the other hand, this study has highlighted limitations for the use of the *RST* algorithm and the instrument. In particular, one of the main identified drawbacks of the method is its computational time, especially for higher frequencies. This is due to its iterative nature and the need for imaging the whole sky in *Lost-in-Space* mode. The time taken to compute this first step will have to be compared to the maximum acceptable delay before engaging the tracking mode.

Also, the peeling process implements sources subtraction that requires to assume isotropic antennas. The design of the antennas may undercut this assumption at frequencies higher than the ones used here. Thus, the frequency range to be used by the *RST* function could be limited by the antenna design.

Furthermore, when imaging with the instrument, the use of a source subtraction algorithm seems inevitable, as the reconstructed images of the sky have shown to be dominated by the brightest bodies no matter the direction. This is due to the secondary lobes and no interferometric imaging method is immune to this. The source subtraction is a major concern. It means that no matter the imaging direction, the interferometer has to provide information on the bright elements of the sky that have to be deconvolved so that the output images are not polluted by the contributions of radio sources in the secondary lobes.

The most critical limitations to the feasibility of the *RST* algorithm are the scattering of the sources and its robustness to bright transient sources.

6 Conclusion

Overall, the algorithm presented in this article has shown its capability to recover the directional information on the sky using only the interferometric visibilities and a radio source catalog. With the mock sky model presented in this study, the algorithm per se shows a potential to reach an accuracy of 1 arcmin and shows, at first, its sensitivity to various parameters. It is able to proceed properly for acquisition with an integration factor $\tau\Delta\nu$ higher than 500, which corresponds, for instance, to a band-width of 10 kHz and an integration time of 5 ms. For reference, the most demanding science objectives require an integration factor of 10^3. Thus, it would be easy for the interferometer to achieve the acquisition parameters identified so that the radio-source tracker can perform well.

The achieved accuracy is encouraging with respect to the scientific requirements of the science at very low frequency. In the case of NOIRE, most science cases require a spatial resolution larger than 1 arcmin. The strongest precision is required for the study of Earth magnetosphere at 10 MHz with an angular resolution of 0.1 arcmin. Thus, if the directional information is given with an accuracy of 1 arcmin, it could be sufficient to generate an image in the right direction that would be recalibrated afterward in order to reach the desired precision.

Nevertheless, the on-board implementation of the *RST* algorithm still needs to address feasibility topics, whose list was identified by this study.

Acknowledgements

This work has been supported by CNES (Centre National d'Études Spatiales). The authors also acknowledge support from Observatoire de Paris-PSL and CNRS (Centre National de la Recherche Scientifique). BS contribution is supported by CENSUS (CEntre pour les Nanosatellites en Sciences de l'UniverS).

Author Contributions

ER developed the methodology and algorithms. BC and JNG provided expertise on radioastronomy and interferometry. BS provided expertise on space system design. ER wrote the initial manuscript version. BC, BS and JNG proofread the manuscript. ER and BC prepared the supplementary material.

Data Availability Statement

The software used to produce the figures of this study is available at `https://gitlab.obspm.fr/erouille/noire_simulation`. The modeling data used for this study (Rouillé et al., 2023) are available on Zenodo at: `https://doi.org/10.5281/zenodo.7603148`.

Notation

$\boldsymbol{c}$ Speed of light in a vacuum
$\boldsymbol{k_B}$ Boltzmann constant
$\boldsymbol{\iota}$ imaginary unit
$\boldsymbol{\Re}$ real part operator
$\boldsymbol{\lambda}$ wavelength
$\boldsymbol{\nu}$ frequency
$\boldsymbol{\Delta\nu}$ frequency bandwidth
$\boldsymbol{\tau}$ integration time
$\boldsymbol{\theta}$ polar angle
$\boldsymbol{\phi}$ azimuthal angle
$\vec{\boldsymbol{r_i}}$ position vector of the satellite i
$\vec{\boldsymbol{b_{i,j}}}$ position vector of the baseline between satellite i and j
$\vec{\boldsymbol{s}}$ direction vector
$\vec{\boldsymbol{k}}$ wave vector
$\boldsymbol{\tau_g}$ time delay
$\boldsymbol{N_{\mathbf{sat}}}$ number of satellite
$\boldsymbol{N_{\mathbf{bl}}}$ number of independent baseline
$\boldsymbol{d_{\mathbf{max}}}$ length of the longest baseline
$\boldsymbol{L}$ antenna length
$\boldsymbol{M_{\mathbf{rot}}}$ rotation matrix
$\boldsymbol{\mathcal{R}_a}$ absolute frame
$\boldsymbol{\mathcal{R}_s}$ system frame
$\boldsymbol{\mathcal{V}_{i,j}}$ interferometric visibility measured with the baseline $\vec{b}_{i,j}$
$\boldsymbol{B(\theta,\phi)}$ brightness map
$\boldsymbol{d\Omega_k}$ elementary solid angle with the direction of $\vec{k}$
$\boldsymbol{\Delta\Omega}$ element of solid angle
$\boldsymbol{\Delta\theta}$ angular resolution
$\boldsymbol{a}$, $\boldsymbol{b}$ angular distance
$\boldsymbol{\gamma}$ bi-angle
$\boldsymbol{L_{\mathbf{mes}}}$ table of geometric properties of the measured sources
$\boldsymbol{L_{\mathbf{cat}}}$ table of geometric properties of the catalog sources
$\boldsymbol{L_{\mathbf{diff}}}$ table of differentiated geometric properties
$\boldsymbol{V}$ table of of the number of vote received by sources pairs
$\boldsymbol{P_\pi}$ permutation matrix sorting the catalog sources in order to match the measured sources
$\boldsymbol{\epsilon}$ error on the rotation matrix
$\boldsymbol{c_{l,m}}$ spherical harmonic coefficients
$\boldsymbol{Y_{l,m}}$ spherical harmonic functions
$\boldsymbol{j_l}$ spherical Bessel functions
$\boldsymbol{\sigma}$ visibility noise amplitude
$\boldsymbol{\alpha}$ noise level
$\boldsymbol{T_{\mathbf{sys}}}$ system temperature
$\boldsymbol{T_A}$ antenna temperature
$\boldsymbol{T_B}$ brightness temperature map
$\boldsymbol{T_{\mathbf{cont}}}$ brightness temperature map of the continuum emissions
$\boldsymbol{T_s}$ brightness temperature of the source s
$\boldsymbol{G}$ antenna gain
$\boldsymbol{\mathcal{A}}$ antenna response
$\boldsymbol{A_{\mathbf{eff}}}$ effective area of the antenna
$\boldsymbol{\eta}$ system efficiency

References

Alexander, J. K., Kaiser, M. L., Novaco, J., Grena, F., & Weber, R. (1975). Scientific instrumentation of the radio-astronomy-explorer-2 satellite. *Astronomy and Astrophysics*, *40*, 365–371.

Arias, M., Vink, J., de Gasperin, F., Salas, P., Oonk, J., Van Weeren, R., ... others (2018). Low-frequency radio absorption in cassiopeia a. *Astronomy & Astrophysics*, *612*, A110.

Carozzi, T. D. (2015, 05). Imaging on a sphere with interferometers: the spherical wave harmonic transform. *Monthly Notices of the Royal Astronomical Society: Letters*, *451*(1), L6-L10. Retrieved from `https://doi.org/10.1093/mnrasl/slv052` doi: 10.1093/mnrasl/slv052

Cecconi, B., Dekkali, M., Briand, C., Segret, B., Girard, J. N., Laurens, A., ... et al. (2018). Noire study report: Towards a low frequency radio interferometer in space. *2018 IEEE Aerospace Conference*. Retrieved from `http://dx.doi.org/10.1109/AERO.2018.8396742` doi: 10.1109/aero.2018.8396742

Chu, X., & Chen, Y. (2018). Time division inter-satellite link topology generation problem: Modeling and solution. *International Journal of Satellite Communications and Networking*, *36*(2), 194–206.

Cong, Y., Yue, B., Xu, Y., Shi, Y., & Chen, X. (2022, December). A New Method of Reconstructing Galactic 3D Structures Using Ultralong-wavelength Radio Observations. *Astrophys. J.*, *940*(2), 180. doi: 10.3847/1538-4357/ac9df7

Cornwell, T. J. (2008). Multiscale clean deconvolution of radio synthesis images. *IEEE Journal of selected topics in signal processing*, *2*(5), 793–801.

de Gasperin, F., Mevius, M., Rafferty, D. A., Intema, H. T., & Fallows, R. A. (2018). The effect of the ionosphere on ultra-low-frequency radio-interferometric observations. *A&A*, *615*, A179. Retrieved from `https://doi.org/10.1051/0004-6361/201833012` doi: 10.1051/0004-6361/201833012

de Gasperin, F., Vink, J., McKean, J. P., Asgekar, A., Avruch, I., Bentum, M. J., ... Zucca, P. (2020). Cassiopeia a, cygnus a, taurus a, and virgo a at ultra-low radio frequencies. *A&A*, *635*, A150. Retrieved from `https://doi.org/10.1051/0004-6361/201936844` doi: 10.1051/0004-6361/201936844

de Oliveira-Costa, A., Tegmark, M., Gaensler, B., Jonas, J., Landecker, T., & Reich, P. (2008). A model of diffuse galactic radio emission from 10 mhz to 100 ghz. *Monthly Notices of the Royal Astronomical Society*, *388*(1), 247–260.

Duisterwinkel, E. H., Dubbelman, G., Demi, L., Talnishnikh, E., Wörtche, H. J., & Bergmans, J. W. (2018). Robust reconstruction of sensor swarms floating through enclosed environments. *Wireless sensor network*, *10*(1), 1–39.

Gorski, K. M., Hivon, E., Banday, A. J., Wandelt, B. D., Hansen, F. K., Reinecke, M., & Bartelmann, M. (2005, apr). HEALPix: A framework for high-resolution discretization and fast analysis of data distributed on the sphere. *The Astrophysical Journal*, *622*(2), 759–771. Retrieved from `https://doi.org/10.1086/427976` doi: 10.1086/427976

Gustafsson, F., & Gunnarsson, F. (2003). Positioning using time-difference of arrival measurements. In *2003 ieee international conference on acoustics, speech, and signal processing, 2003. proceedings. (icassp '03).* (Vol. 6, p. VI-553). doi: 10.1109/ICASSP.2003.1201741

Huynh, D. Q. (2009). Metrics for 3d rotations: Comparison and analysis. *Journal of Mathematical Imaging and Vision*, *35*(2), 155–164.

Högbom, J. (1974). Aperture synthesis with a non-regular distribution of interferometer baselines. *Astronomy and Astrophysics Supplement Series*, *15*, 417.

Jester, S., & Falcke, H. (2009). Science with a lunar low-frequency array: From the dark ages of the universe to nearby exoplanets. *New Astronomy Reviews*, *53*(1), 1-26. Retrieved from `https://www.sciencedirect.com/science/article/pii/S1387647309000086` doi: https://doi.org/10.1016/j.newar.2009.02.001

Kasper, J., Lazio, J., Romero-Wolf, A., Lux, J., & Neilsen, T. (2021). The sun radio interferometer space experiment (sunrise) mission. In *2021 ieee aerospace conference (50100)* (p. 1-11). doi: 10.1109/AERO50100.2021.9438184

Kim, K., & Bang, H. (2020). Algorithm with patterned singular value approach for highly reliable autonomous star identification. *Sensors*, *20*(2). Retrieved from `https://www.mdpi.com/1424-8220/20/2/374` doi: 10.3390/s20020374

Kolomenkin, M., Pollak, S., Shimshoni, I., & Lindenbaum, M. (2008). Geometric voting algorithm for star trackers. *IEEE Transactions on Aerospace and Electronic Systems*, *44*(2), 441–456.

Liebe, C. (1995). Star trackers for attitude determination. *IEEE Aerospace and Electronic Systems Magazine*, *10*(6), 10-16. doi: 10.1109/62.387971

McKean, J., Godfrey, L., Vegetti, S., Wise, M. W., Morganti, R., Hardcastle, M., ... others (2016). Lofar imaging of cygnus a–direct detection of a turnover in the hotspot radio spectra. *Monthly Notices of the Royal Astronomical Society*, *463*(3), 3143–3150.

Novaco, J. C., & Brown, L. W. (1978). Nonthermal galactic emission below 10 megahertz. *The Astrophysical Journal*, *221*, 114–123.

Oberoi, D., & Pinçon, J. (2003). A new design for a very low frequency satellite based radio interferometer. In *Agu fall meeting abstracts* (Vol. 2003, pp. SH42C–0552).

Rajan, R. T., & van der Veen, A.-J. (2015). Joint ranging and synchronization for an anchorless network of mobile nodes. *IEEE Transactions on Signal Processing*, *63*(8), 1925–1940.

Rouillé, E., Cecconi, B., Segret, B., & Girard, J. N. (2023). *Radio-Source Tracker: Autonomous Attitude Determination on a Radio Interferometric Swarm: supplementary dataset.* Zenodo. doi: 10.5281/zenodo.7603149

Scaife, A. M. M., & Heald, G. H. (2012, June). A broad-band flux scale for low-frequency radio telescopes. *Mon. Notices Royal Astron. Soc.*, *423*(1), L30-L34. doi: 10.1111/j.1745-3933.2012.01251.x

Stanislavsky, L. A., Bubnov, I. N., Konovalenko, A. A., Stanislavsky, A. A., & Yerin, S. N. (2022). *Free-free absorption parameters of cassiopeia a from low-frequency interferometric observations.* arXiv. Retrieved from `https://arxiv.org/abs/2212.06104` doi: 10.48550/ARXIV.2212.06104

Steer, D., Dewdney, P., & Ito, M. (1984). Enhancements to the deconvolution algorithm'clean'. *Astronomy and Astrophysics*, *137*, 159–165.

Stuart, J., Dorsey, A., Alibay, F., & Filipe, N. (2017). Formation flying and position determination for a space-based interferometer in geo graveyard orbit. In *2017 ieee aerospace conference* (p. 1-19). doi: 10.1109/AERO.2017.7943705

Taylor, G. B., Carilli, C. L., & Perley, R. A. (1999). Synthesis imaging in radio astronomy ii. *A Collection of Lectures from the Sixth NRAO/NMIMT Synthesis Imaging Summer School*, *180*.

Thompson, A. R., Moran, J. M., & Swenson, G. W. (2017). *Interferometry and synthesis in radio astronomy.* Springer Nature.

van Haarlem, M. P., Wise, M. W., Gunst, A. W., Heald, G., McKean, J. P., Hessels, J. W. T., ... et al. (2013, August). LOFAR: The LOw-Frequency ARray. *Astrophys. J. Suppl. Series*, *556*, A2. doi: 10.1051/0004-6361/201220873

Vinyaikin, E., Nikonov, V., Tarasov, A., Tokarev, Y. V., & Yurishchev, M. (1987). Spectrum of low-frequency radio emission of cassiopeia-a. *Soviet Astronomy*, *31*, 517.

Zarka, P. (2004). Fast radio imaging of jupiter's magnetosphere at low-frequencies with lofar. *Planetary and Space Science*, *52*(15), 1455-1467. Retrieved from `https://www.sciencedirect.com/science/article/pii/S003206330400145X` doi: https://doi.org/10.1016/j.pss.2004.09.017

Zarka, P., Bougeret, J.-L., Briand, C., Cecconi, B., Falcke, H., Girard, J., ... others (2012). Planetary and exoplanetary low frequency radio observations from the

moon. *Planetary and Space Science*, *74*(1), 156–166.
Zarka, P., Girard, J. N., Tagger, M., & Denis, L. (2012, December). LSS/NenuFAR: The LOFAR Super Station project in Nançay. In S. Boissier, P. de Laverny, N. Nardetto, R. Samadi, D. Valls-Gabaud, & H. Wozniak (Eds.), *Sf2a-2012: Proceedings of the annual meeting of the french society of astronomy and astrophysics* (p. 687-694).
Zonca, A., Singer, L. P., Lenz, D., Reinecke, M., Rosset, C., Hivon, E., & Gorski, K. M. (2019). healpy: equal area pixelization and spherical harmonics transforms for data on the sphere in python. *Journal of Open Source Software*, *4*(35), 1298.

Appendix A Visibility equation

The electric field observed at position $\vec{r_i}$ propagating in the direction $\vec{k}$ at the frequency ν can be expressed as

$$\tilde{E}_{\nu,i}(\Omega_k, t) = E \exp(\iota(2\pi\nu t - \vec{k}\cdot\vec{r_i} + \phi)) \tag{A1}$$

Then, the signal received by an antenna at the position $\vec{r_i}$ is expressed as follows:

$$V_{\nu,i}(t) = \iint \mathcal{A}(\Omega_k)\ \tilde{E}_{\nu,i}(\Omega_k, t)\ d\Omega_k \tag{A2}$$

where $\mathcal{A}$ is the antenna gain. The antenna response is supposed to be omnidirectional. Thus, $\mathcal{A} = 1$. Also, the bandwidth is supposed to be thin so the subscript $\bullet_\nu$ is removed later on.

The correlation between two antennas is then:

$$\begin{aligned}
\mathcal{V}_{i,j} &= \langle V_i . V_j^* \rangle \\
&= \left\langle \Big(\iint \tilde{E}(\Omega_k, t) d\Omega_k \Big) . \Big(\iint \tilde{E}(\Omega'_k, t) d\Omega_{k'} \Big)^\star \right\rangle \\
&= \left\langle \iint \iint \tilde{E}(\Omega_k, t) \tilde{E}^*(\Omega'_k, t) d\Omega_k d\Omega_{k'} \right\rangle \\
&= \iint \iint \underbrace{\left\langle E(\Omega_k, t) . E^*(\Omega'_k, t) \right\rangle}_{=0 \text{ if } \Omega_k \neq \Omega_{k'}} .\ \exp\big(-\iota((\vec{k}\cdot\vec{x_i}) - (\vec{k'}\cdot\vec{x_j}))\big)\ d\Omega_k d\Omega_{k'} \\
&= \iint \langle \|E(\Omega_k, t)\|^2 \rangle\ .\ \exp\big(-\iota\vec{k}\cdot(\vec{x_i} - \vec{x_j})\big) d\Omega_k \\
&\propto \iint B(\Omega_k, t)\ .\ \exp\big(-\iota\vec{k}\cdot\vec{b_{i,j}}\big) d\Omega_k
\end{aligned} \tag{A3}$$

where $\langle \bullet \rangle$ is the time average operator. With the assumption that the radiation from astronomical objects is not spatially coherent; i.e., that $\langle E(\Omega_k) E^\star(\Omega_{k'}) \rangle = 0$ for $\Omega_k \neq \Omega_{k'}$.

Appendix B Omni-directional Antenna

The signal received on an antenna is expressed as:

$$V = \iint \mathcal{A}(\Omega_k) E(\Omega_k) d\Omega \tag{B1}$$

where $E(\Omega_k)$ is the electric field whose wave vector direction is $\vec{k}$ and $\mathcal{A}$ is the antenna gain.

The power received by that antenna is its auto-correlation expressed as follows:

$$\begin{aligned}
A &= \langle VV^\star \rangle \\
&= \left\langle \Big(\iint \mathcal{A}(\Omega_k) E(\Omega_k) d\Omega_k \Big) \Big(\iint \mathcal{A}(\Omega_{k'}) E(\Omega_{k'}) d\Omega'_k \Big)^\star \right\rangle \\
&= \left\langle \iint \iint \mathcal{A}(\Omega_k) E(\Omega_k) \mathcal{A}(\Omega_{k'}) E^\star(\Omega_{k'}) d\Omega_k d\Omega_{k'} \right\rangle \\
&= \iint \iint \mathcal{A}(\Omega_k)\mathcal{A}(\Omega_{k'}) \underbrace{\left\langle E(\Omega_k) E^\star(\Omega_{k'}) \right\rangle}_{=0 \text{ if } \Omega_k \neq \Omega_{k'}} d\Omega_k d\Omega_{k'} \\
&= \iint \mathcal{A}^2(\Omega_k) \langle \|E(\Omega_k)\|^2 \rangle d\Omega
\end{aligned} \tag{B2}$$

In the case of a dipole antenna of direction $\vec{n}$ in the short dipole regime, it verifies:

$$\mathcal{A}_n(\Omega_s) = \|\vec{n} \times \vec{s}\| \tag{B3}$$

with $\vec{s} = \vec{k}/\|k\|$ the direction of propagation.

The power it received is expressed as:

$$\begin{aligned}
A_n &= \langle V_n V_n^\star \rangle \\
&= \iint \|\vec{n} \times \vec{s}\|^2 \langle \|E(\Omega_k)\|^2 \rangle d\Omega \\
&= \iint (1 - (\vec{n} \cdot \vec{s})^2) \langle \|E(\Omega_k)\|^2 \rangle d\Omega
\end{aligned} \tag{B4}$$

We used the property $(\vec{n} \times \vec{s}) \cdot (\vec{n} \times \vec{s}) = (\vec{n} \cdot \vec{n})(\vec{s} \cdot \vec{s}) - (\vec{n} \cdot \vec{s})(\vec{s} \cdot \vec{n}) = 1 - (\vec{n} \cdot \vec{s})^2$

Then the sum of three orthogonal dipoles is:

$$\begin{aligned}
A &= A_x + A_y + A_z \\
&= \iint \langle \|E(\Omega_k)\|^2 \rangle \Big(1 - (\vec{x} \cdot \vec{s})^2 + 1 - (\vec{y} \cdot \vec{s})^2 + 1 - (\vec{z} \cdot \vec{s})^2 \Big) d\Omega \\
&= \iint \langle \|E(\Omega_k)\|^2 \rangle \Big(3 - ((\vec{x} \cdot \vec{s})^2 + (\vec{y} \cdot \vec{s})^2 + (\vec{z} \cdot \vec{s})^2) \Big) d\Omega \\
&= \iint \langle \|E(\Omega_k)\|^2 \rangle \Big(3 - \|\vec{s}\|^2 \Big) d\Omega \\
&= \iint \langle \|E(\Omega_k)\|^2 \rangle (3 - 1) d\Omega \\
&= \iint 2 \langle \|E(\Omega_k)\|^2 \rangle d\Omega
\end{aligned} \tag{B5}$$

which is equivalent to an omnidirectional antenna of gain 2.

For the sake of the simulation, every satellite is considered to behave as an isotropic antenna of gain 1. The only thing impacted is the effective area of the antenna considered for the noise level calculation. $A_{\text{eff}} = \lambda^2/(4\pi)$ is used instead of $A_{\text{eff}} = 3\lambda^2/(8\pi) \times 3$.

Appendix C SWHT

The full sky can be expanded as a linear combination of spherical harmonic as:

$$B(\Omega_k) = \sum_{l=0}^{\infty} \sum_{m=-l}^{l} c_{l,m} Y_{l,m}(\Omega_k) \tag{C1}$$

where $Y_{l,m}$ are the standard, orthonormal spherical harmonic functions with l and m corresponding to the polar and azimuthal quantal numbers. The coefficients $c_{l,m}$ are given by:

$$c_{l,m} = \iint B(\Omega_k) Y^*_{l,m}(\Omega_k) d\Omega \tag{C2}$$

Following Carozzi (2015), the visibility domain can be expressed into spherical wave harmonics, which leads to the following equation for a baseline $\vec{b}$:

$$\mathcal{V}(\vec{b}) = 4\pi \sum_{l=0}^{\infty} \sum_{m=-l}^{l} (-\iota)^l j_l(kr_b) Y_{l,m}(\theta_b, \phi_b) c_{l,m} \tag{C3}$$

where j_l are the spherical Bessel functions of the first kind and (r_b, θ_b, ϕ_b) is the spherical representation of the vector $\vec{b}$.

The spherical harmonic coefficient can be estimated using a discretization:

$$c_{l,m} \simeq \sum_{\vec{k}} B(\Omega_k) Y^*_{l,m}(\Omega_k) \Delta\Omega \tag{C4}$$

This equation is valid if the sampling step is smaller than the typical scale of the structures in the sky.

Similarly, the quantal numbers representing spatial elements smaller than the sampling step are negligible. Thus, the linear combination can be truncated to a maximum polar number l_{max}. The spatial elements represented as such are no larger than $\Delta\theta = \pi/l_{max}$ Therefore, it is possible to estimate the measured visibility for a given baseline $\vec{b}$ by decomposing the sky into its spherical components.

What is interesting with this method is the way the sky is decomposed. With the spherical components, the scale of the sampling is constrained by the scale of brightness fluctuations in the sky. Whereas, the sampling used in the Eq. 13 is constrained by the resolution of the instrument. For that reason, the SWHT method is convenient to simulate the visibility induced by the diffuse emission when the resolution of the instrument is considerably smaller than the scale of the brightness fluctuation of the diffuse sky.

Appendix D Choice of the Factor 8 Between ν_1 and ν_2

A first image of the full sky is generated. Its size is $\Omega_1 = 4\pi$ sr and its resolution is $\Delta\theta_1 = c/(D\nu_1)$, its number of pixel is:

$$N_{\text{pix},1} = \frac{\Omega_1}{{\Delta\theta_1}^2} = 4\pi \big(\frac{D}{c}\big)^2 \nu_1^2 \tag{D1}$$

The second image is generated with a radius of $\sqrt{\Omega_2} = 5\Delta\theta_1$. Its resolution is $\Delta\theta_2 = c/(D\nu_2)$. Then, its number of pixel is:

$$N_{\text{pix},2} = \Big(\frac{\sqrt{\Omega_2}}{\Delta\theta_2}\Big)^2 = (5\nu_2/\nu_1)^2 \tag{D2}$$

The total number of pixel can expressed as:

$$\begin{aligned} N_{\text{pix, tot}} &= 4\pi\Big(\frac{D}{c}\Big)^2\nu_1^2 + 5^2\Big(\frac{\nu_2}{\nu_1}\Big)^2 \\ &= 4\pi\Big(\frac{D}{c}\Big)^2\Big(\frac{\nu_2}{\alpha}\Big)^2 + 5^2\alpha^2 \end{aligned} \tag{D3}$$

with $\alpha = \nu_2/\nu_1$ defining the factor between the two frequencies.

Let's suppose that ν_2 is fixed in order to achieve a specific resolution, then the factor α can be selected in order to minimize the number of pixel computed:

$$\begin{aligned} &\frac{\partial N_{\text{pix, tot}}}{\partial\alpha} = 0 \\ &\iff -8\pi\Big(\frac{D}{c}\Big)^2\nu_2^2\frac{1}{\alpha^3} + 50\alpha = 0 \\ &\iff \alpha^4 = 8\pi\Big(\frac{D}{c}\Big)^2\nu_2^2\frac{1}{50} \\ &\iff \alpha = (4\pi)^{1/4}\sqrt{\frac{D\nu_2}{5c}} \end{aligned} \tag{D4}$$

For $D = 100$km and $\nu_2 = 300$kHz, one has $\alpha = 8.42$.

As the Healpix map resolution evolves as a power of 2, a factor of $8 = 2^3$ matches. It means that the resolution at ν_2 is 3 order smaller than the one at ν_1. For this reason, the factor between ν_2 and ν_1 is set to 8.

Appendix E Doppler Effect

The Doppler effect described how a relative velocity induces a shift in frequency.

As the satellites have relative velocity, they do not observe the same frequency in a given direction. The relative velocities in a 100-kilometer swarm around the moon are supposed to be lower than 100m/s. With this velocity, the relative frequency shift does not exceed $\frac{\delta\nu}{\nu} = 3.4 \times 10^{-7}$. For instance, at 1MHz, that is a shift of 0.3Hz which is negligible compare to the bandwidth which is expected to be closer to 5kHz.

Therefore, when observing in a given direction, the Doppler effect induces by the relative velocity can be neglected.

Appendix F Reflection Matrices

A reflection matrix $\boldsymbol{R}$ is defined by

$\boldsymbol{R}\cdot\boldsymbol{R}^t = I \; det(\boldsymbol{R}) = -1$

they verify $\boldsymbol{R}^{-1} = \boldsymbol{R}^t$

Let $\boldsymbol{R}_1$ and $\boldsymbol{R}_2$ be two reflection matrices. let define $\boldsymbol{M} = \boldsymbol{R}_1\cdot\boldsymbol{R}_2^{-1}$

$\boldsymbol{M}\cdot\boldsymbol{M}^t = \boldsymbol{R}_1\cdot\boldsymbol{R}_2^{-1}\cdot\boldsymbol{R}_2\cdot\boldsymbol{R}_1^{-1} = \boldsymbol{R}_1\cdot I\cdot\boldsymbol{R}_1^{-1} = I$

$det(\boldsymbol{M}) = det(\boldsymbol{R}_1\cdot\boldsymbol{R}_2^{-1}) = det(\boldsymbol{R}_1)/det(\boldsymbol{R}_2) = -1/-1 = 1$

Thus, $\boldsymbol{M}$ is a rotation.

This proves that for a given reflection matrix $\boldsymbol{R}_2$ and for any reflection matrix $\boldsymbol{R}_1$, there exists a rotation matrix $\boldsymbol{M}$ so that $\boldsymbol{R}_1 = \boldsymbol{M} \cdot \boldsymbol{R}_2$

Figure 1.

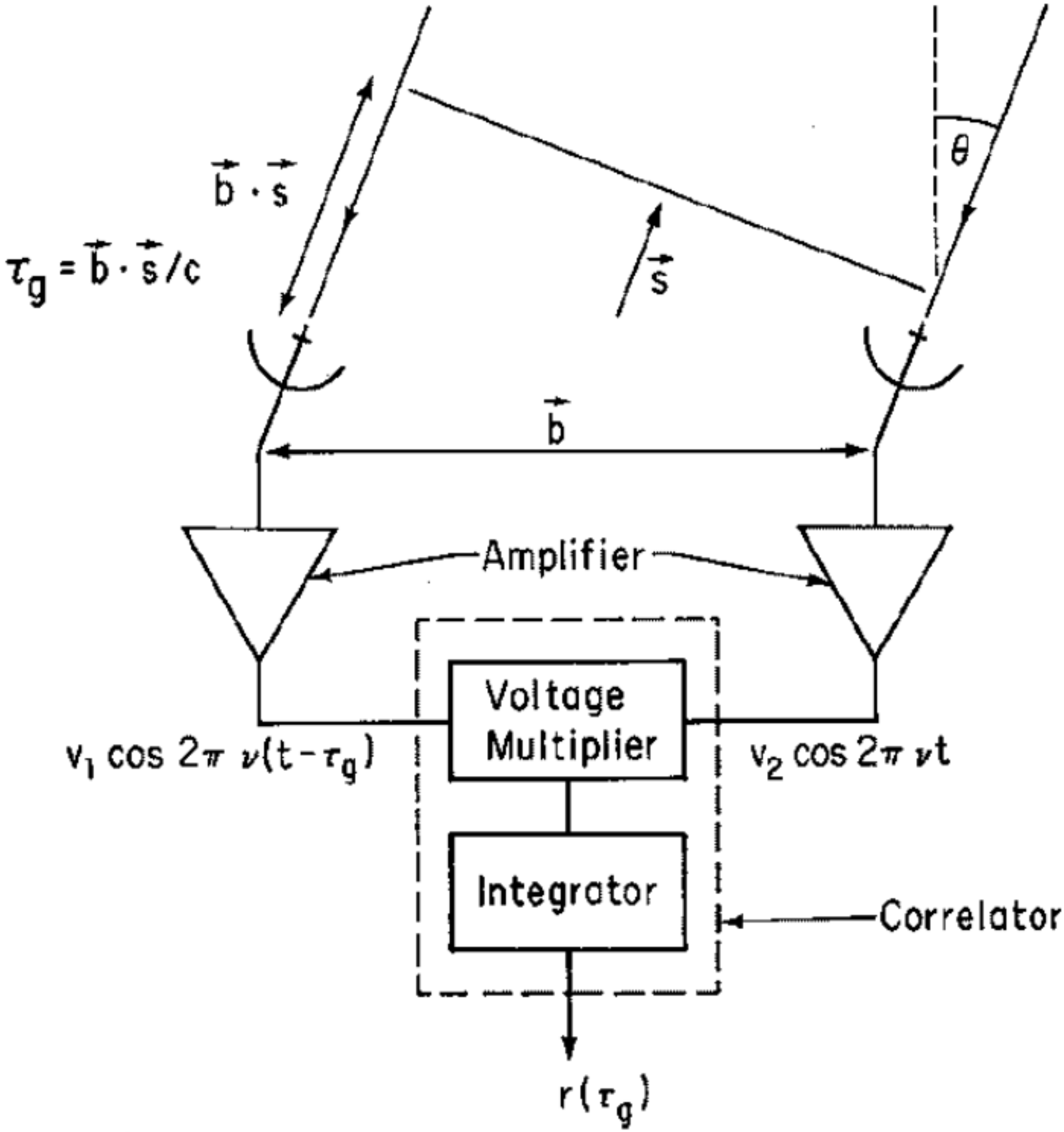
$\vec{b} \cdot \vec{s}$
$\tau_g = \vec{b} \cdot \vec{s}/c$
$\vec{s}$
θ
$\vec{b}$
Amplifier
Voltage Multiplier
Integrator
Correlator
$v_1 \cos 2\pi \nu(t-\tau_g)$
$v_2 \cos 2\pi \nu t$
$r(\tau_g)$

Figure 2.

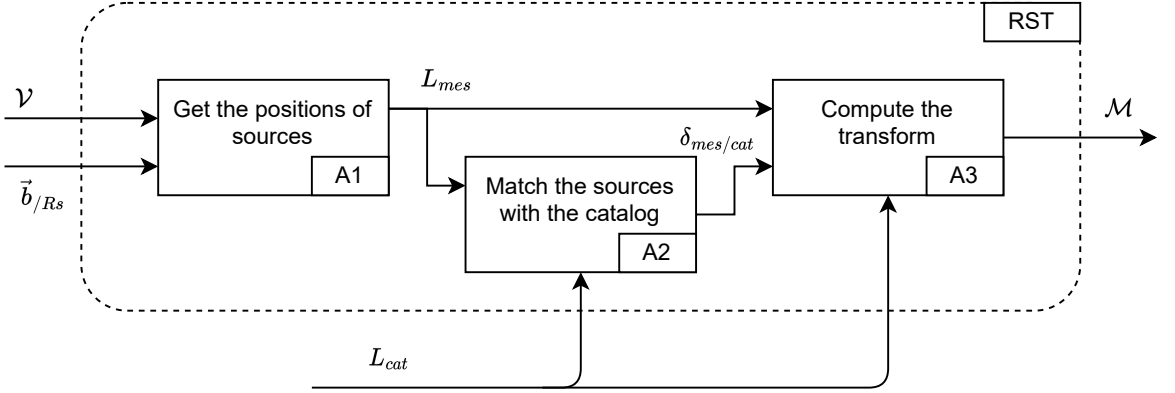
RST
$\mathcal{V}$
$\vec{b}_{/Rs}$
Get the positions of sources
A1
L_{mes}
Match the sources with the catalog
A2
$\delta_{mes/cat}$
Compute the transform
A3
$\mathcal{M}$
L_{cat}

Figure 3.

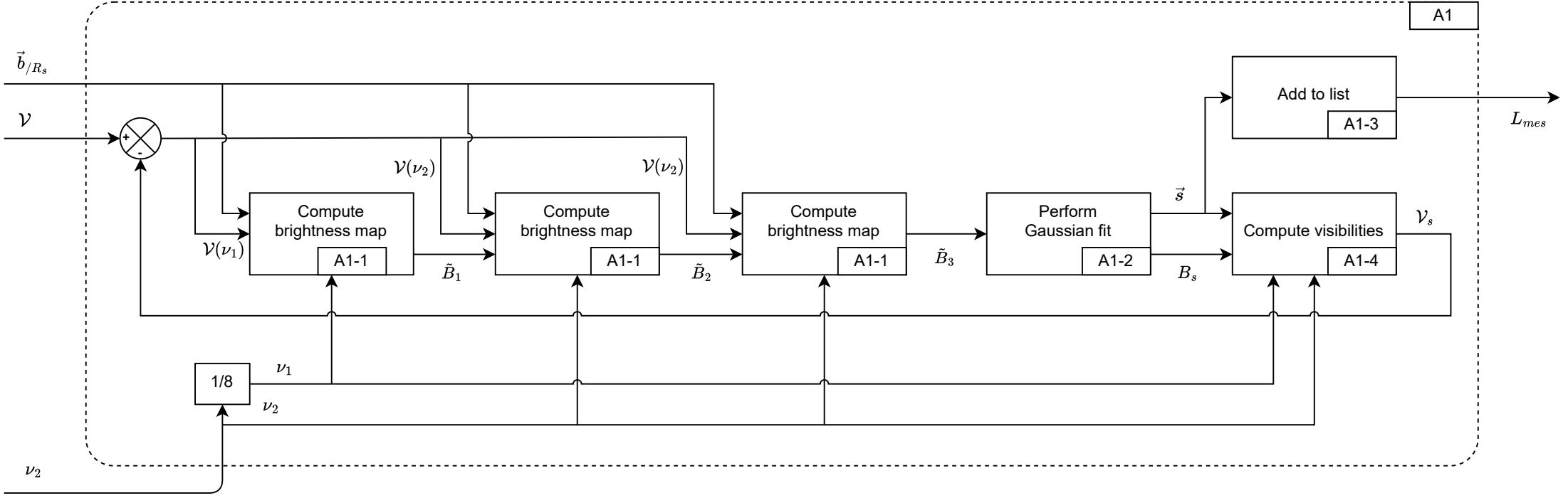
A1
$\vec{b}_{/R_s}$
$\mathcal{V}$
+
-
$\mathcal{V}(\nu_1)$
$\mathcal{V}(\nu_2)$
$\mathcal{V}(\nu_2)$
Compute brightness map
A1-1
$\tilde{B}_1$
Compute brightness map
A1-1
$\tilde{B}_2$
Compute brightness map
A1-1
$\tilde{B}_3$
Perform Gaussian fit
A1-2
$\vec{s}$
B_s
Add to list
A1-3
L_{mes}
Compute visibilities
A1-4
$\mathcal{V}_s$
1/8
ν_1
ν_2
ν_2

Figure 4a.

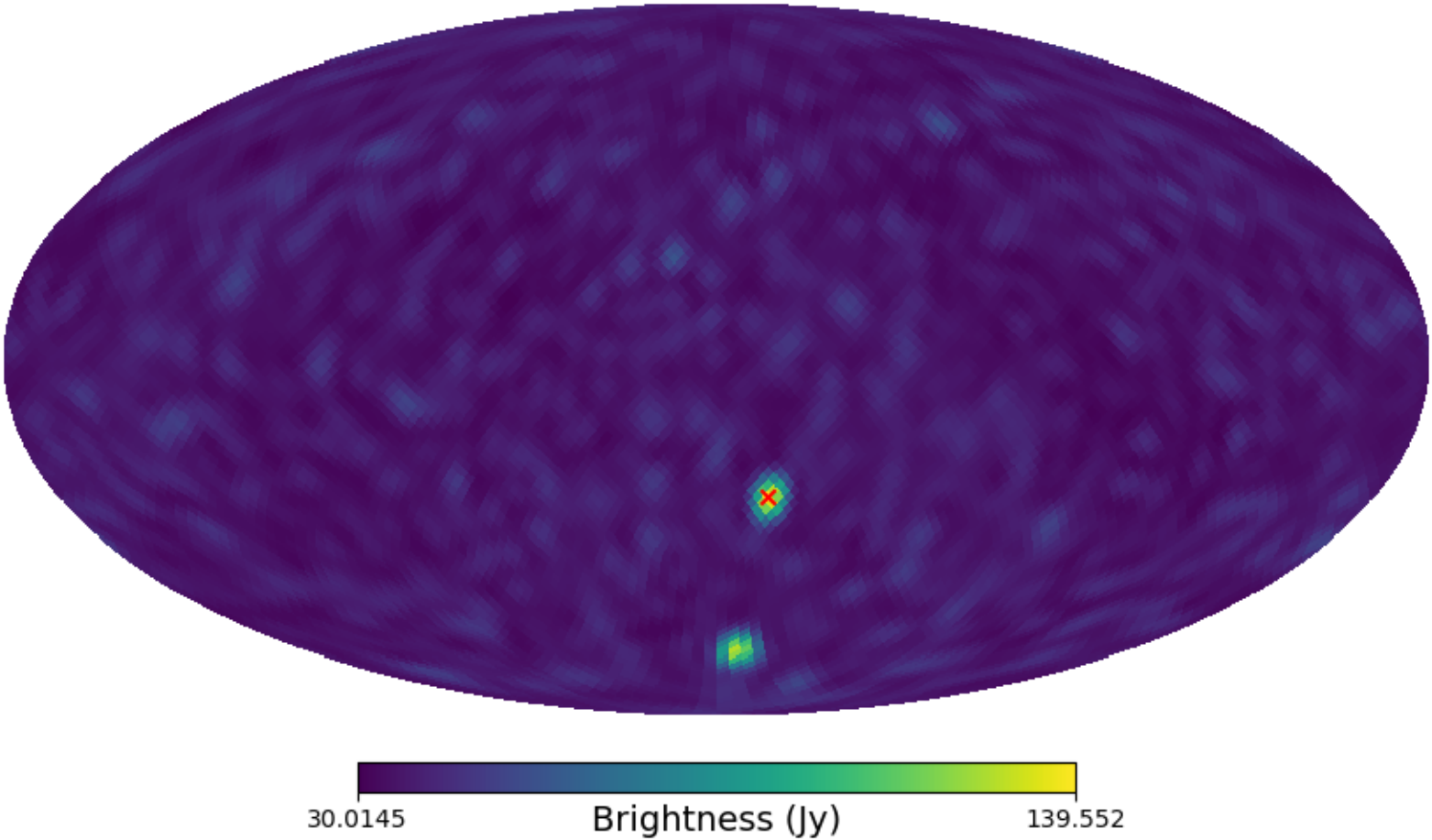
30.0145
Brightness (Jy)
139.552

Figure 4b.

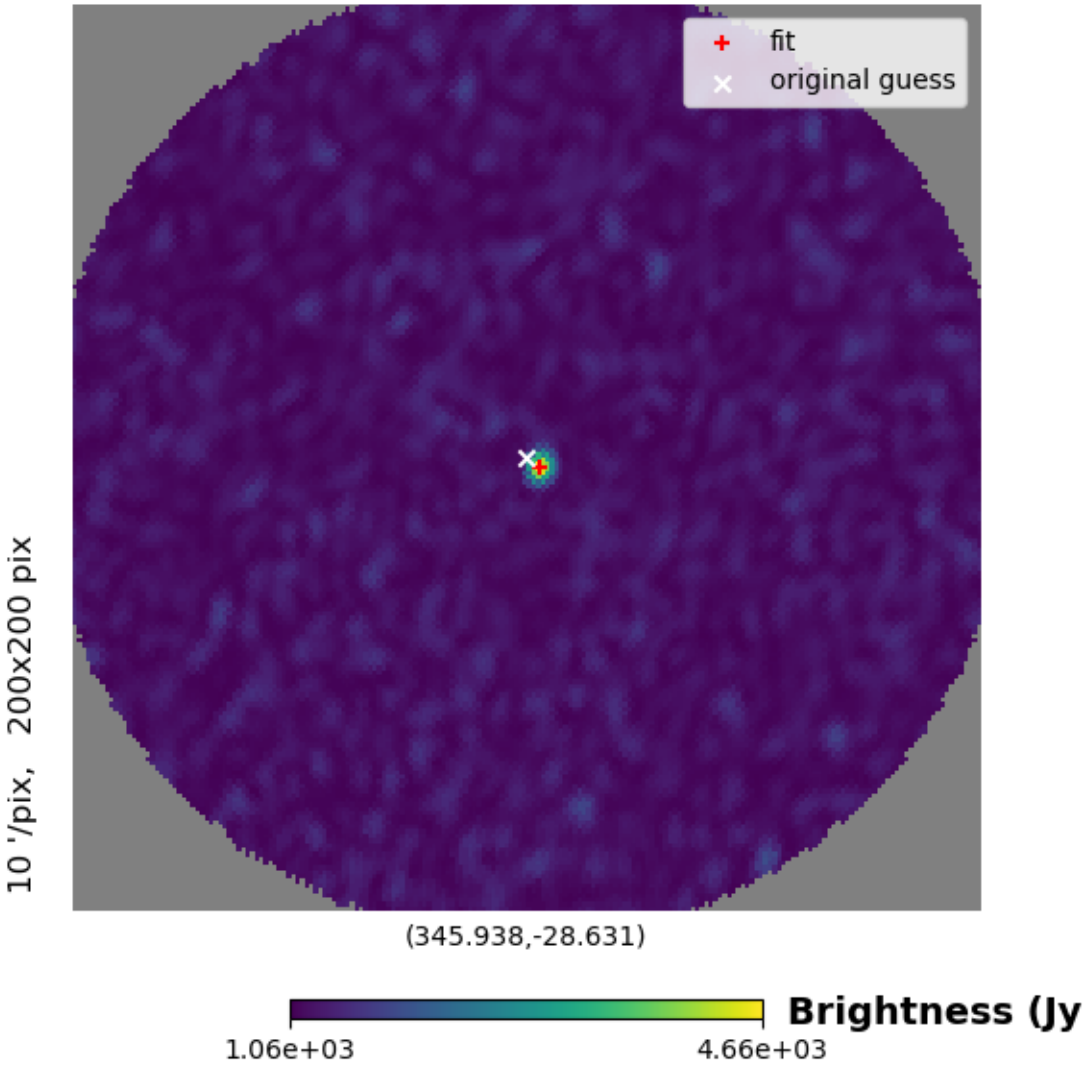
fit
original guess
10 '/pix, 200x200 pix
(345.938,-28.631)
Brightness (Jy
1.06e+03
4.66e+03

Figure 4c.

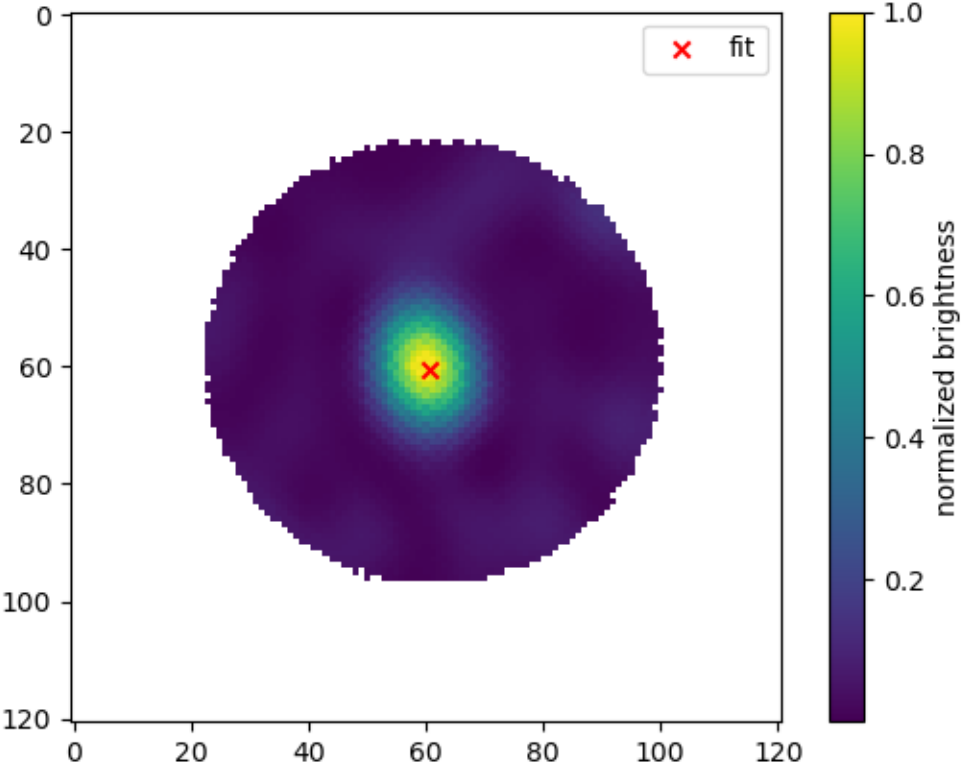
fit
0
20
40
60
80
100
120
normalized brightness
1.0
0.8
0.6
0.4
0.2

Figure 5.

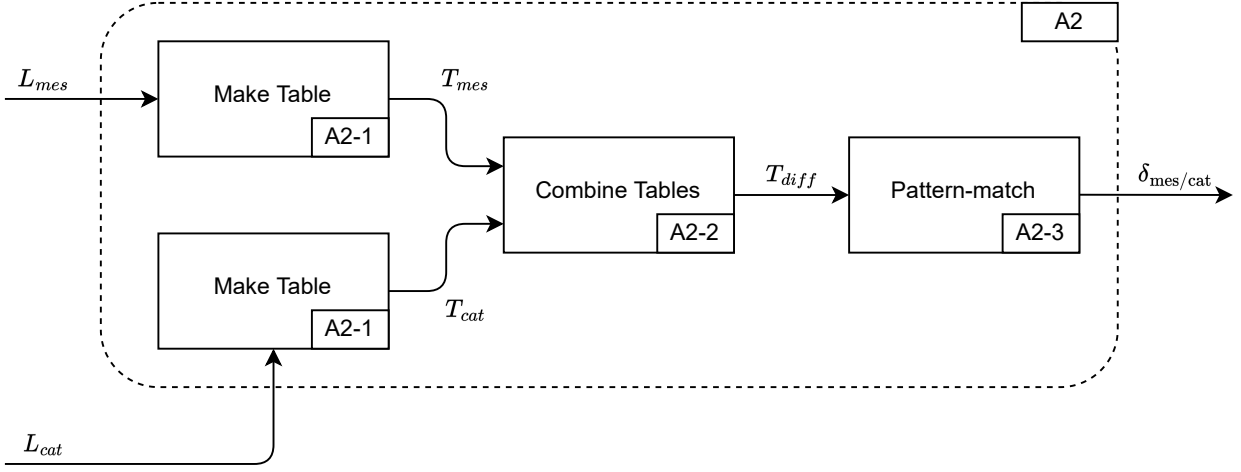
A2
L_{mes}
Make Table
A2-1
T_{mes}
Combine Tables
A2-2
T_{diff}
Pattern-match
A2-3
$\delta_{\mathrm{mes/cat}}$
Make Table
A2-1
T_{cat}
L_{cat}

Figure 6.

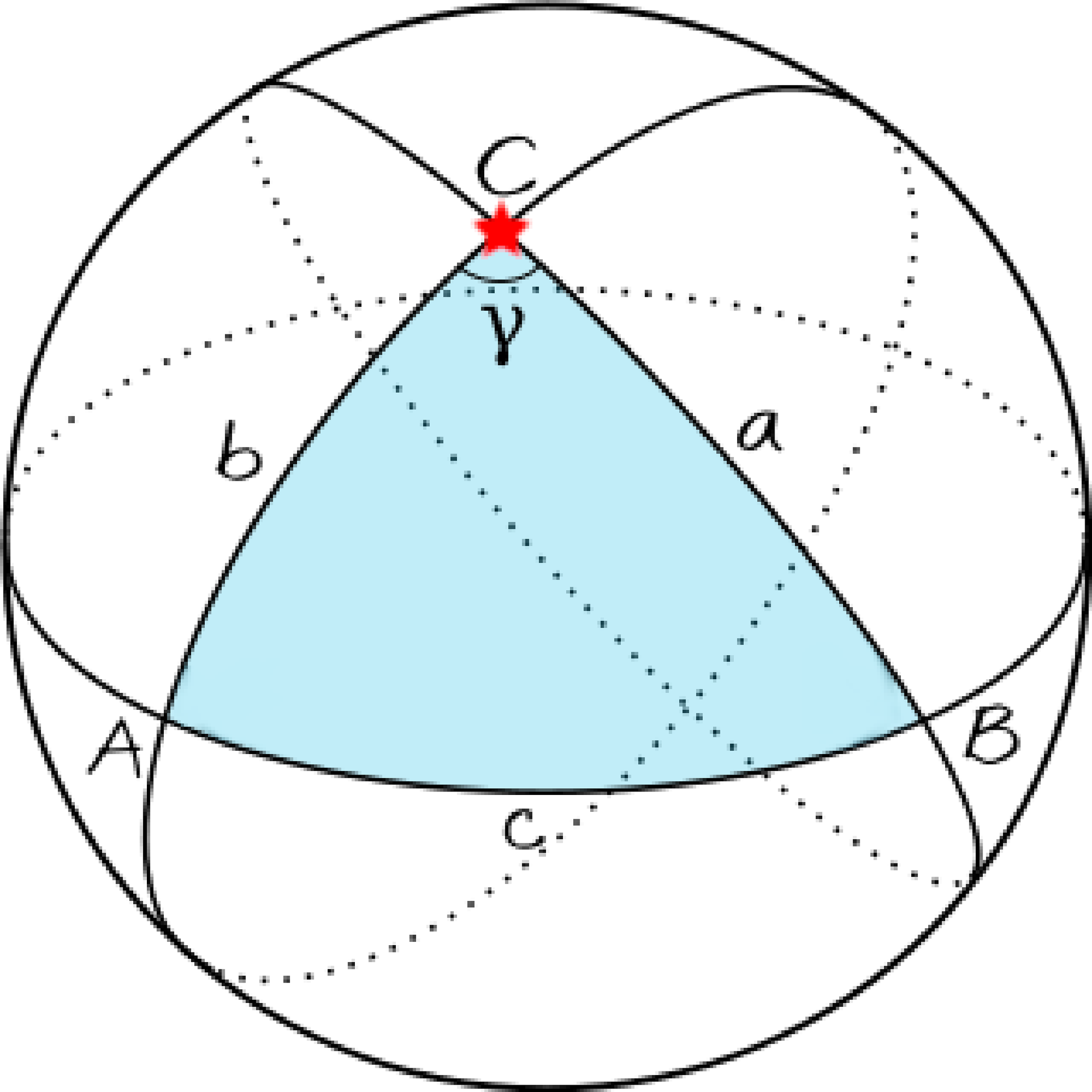
C
γ
b
a
A
B
c

Figure 7.

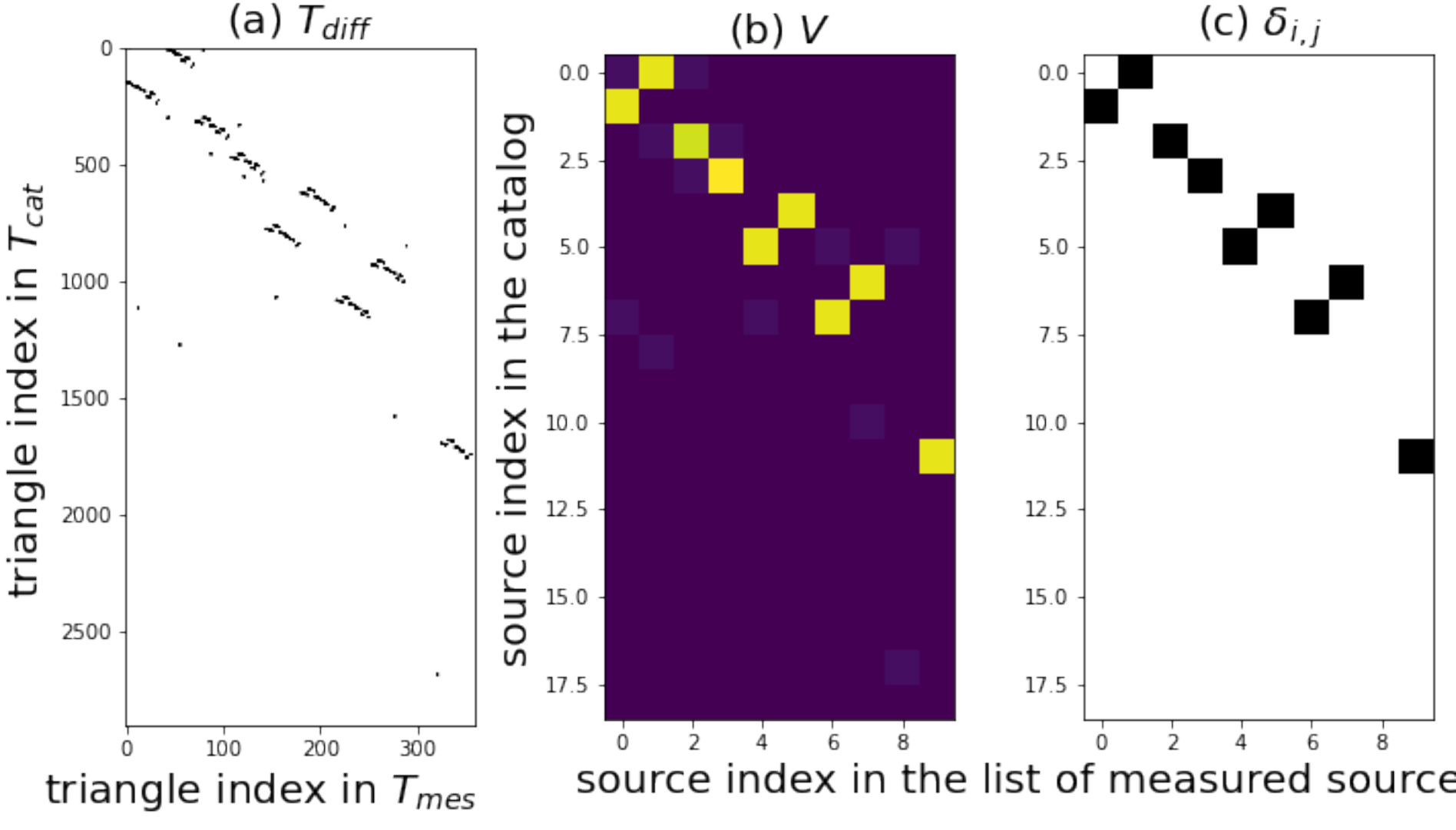
(a) T_{diff}
triangle index in T_{cat}
triangle index in T_{mes}
0
500
1000
1500
2000
2500
0
100
200
300
(b) V
source index in the catalog
source index in the list of measured source
0.0
2.5
5.0
7.5
10.0
12.5
15.0
17.5
0
2
4
6
8
(c) $\delta_{i,j}$
0.0
2.5
5.0
7.5
10.0
12.5
15.0
17.5
0
2
4
6
8

Figure 8.

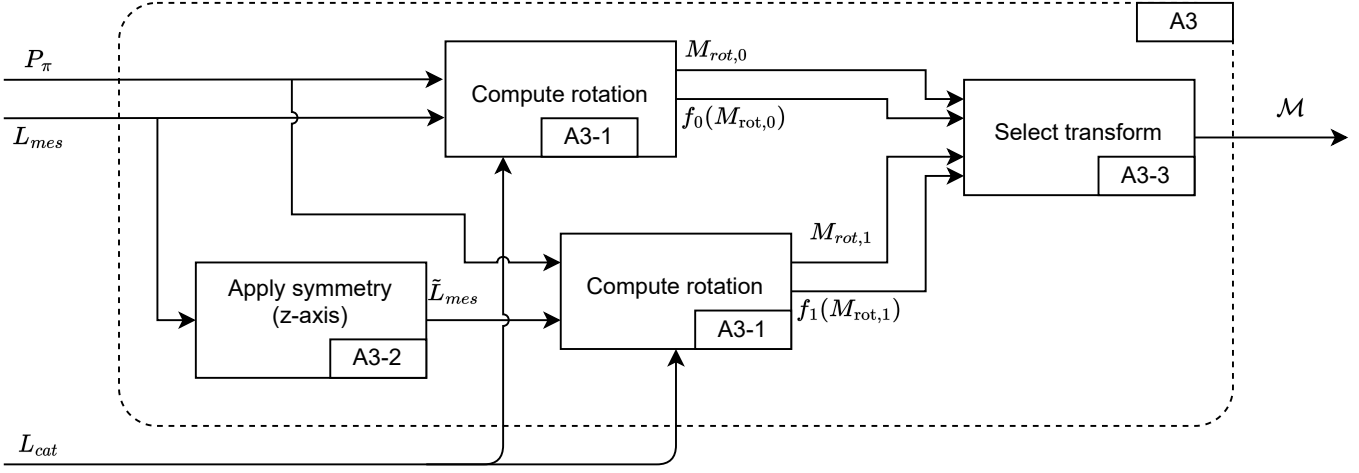
A3
P_π
L_{mes}
Compute rotation
A3-1
$M_{rot,0}$
$f_0(M_{\mathrm{rot},0})$
Select transform
A3-3
$\mathcal{M}$
$M_{rot,1}$
Apply symmetry
(z-axis)
A3-2
$\tilde{L}_{mes}$
Compute rotation
A3-1
$f_1(M_{\mathrm{rot},1})$
L_{cat}

Figure 9a.

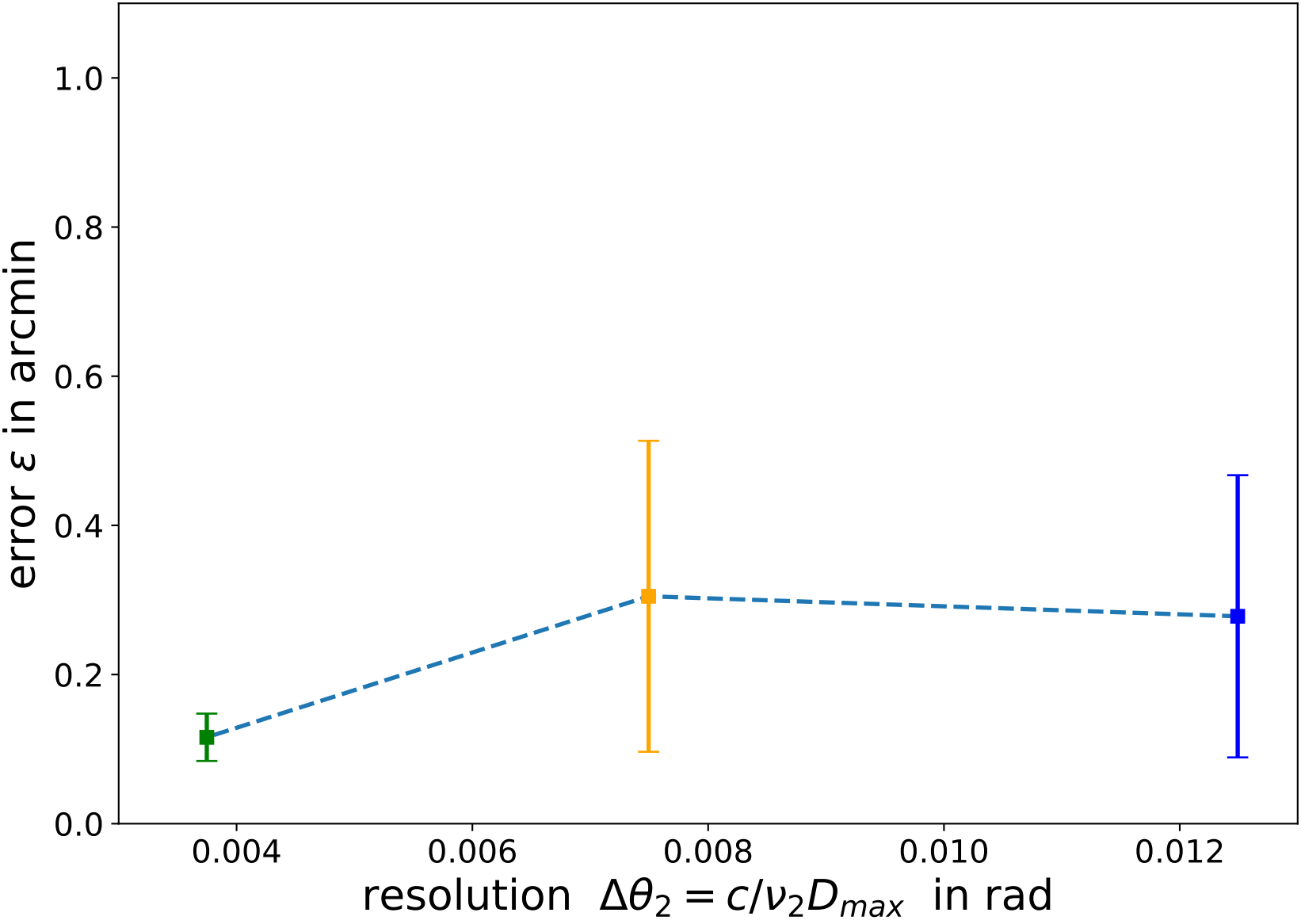
1.0
0.8
0.6
0.4
0.2
0.0
error ε in arcmin
0.004
0.006
0.008
0.010
0.012
resolution $\Delta\theta_2 = c/\nu_2 D_{max}$ in rad

Figure 9b.

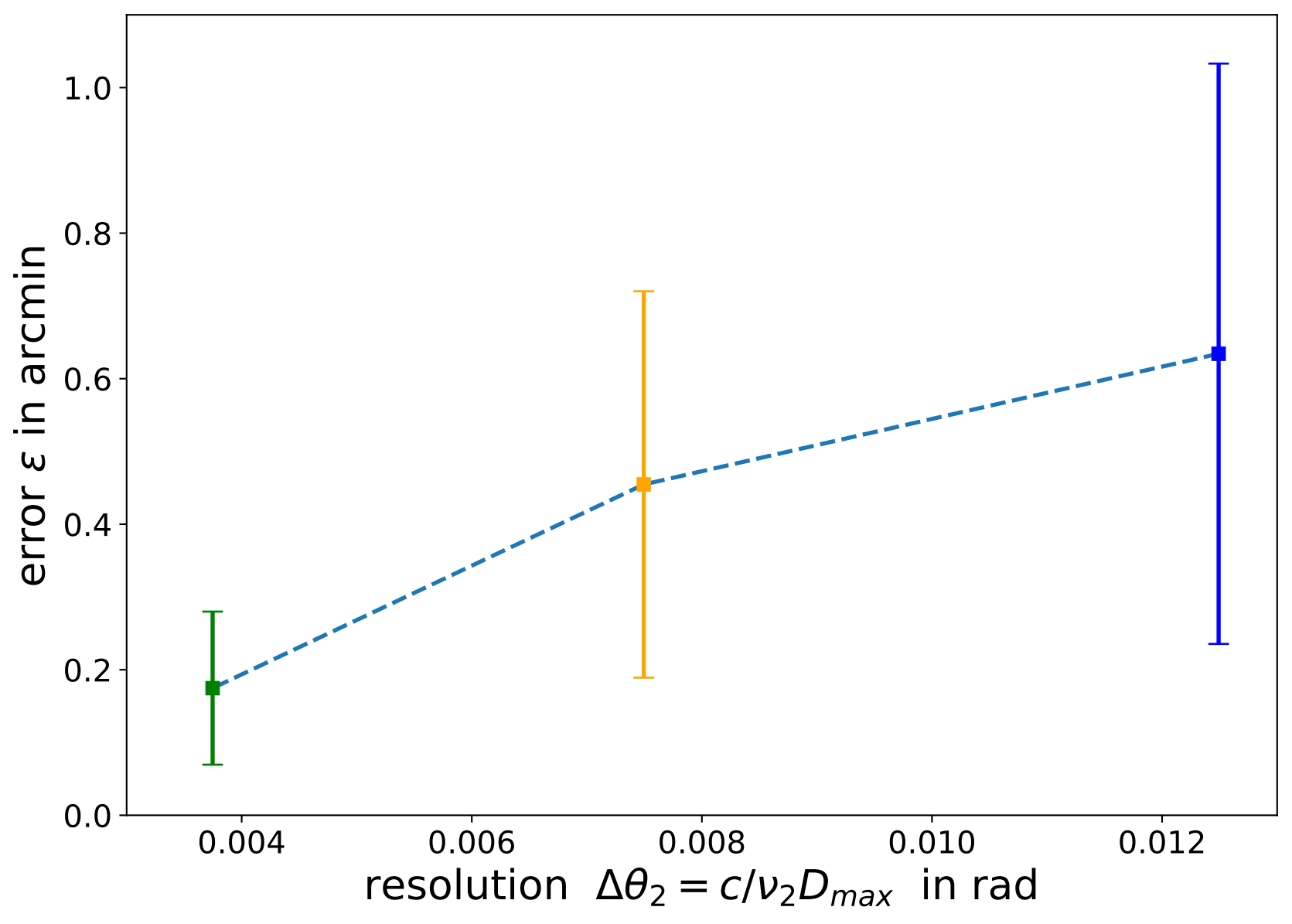
1.0
0.8
0.6
0.4
0.2
0.0
error ε in arcmin
0.004
0.006
0.008
0.010
0.012
resolution $\Delta\theta_2 = c/\nu_2 D_{max}$ in rad

Figure 10.

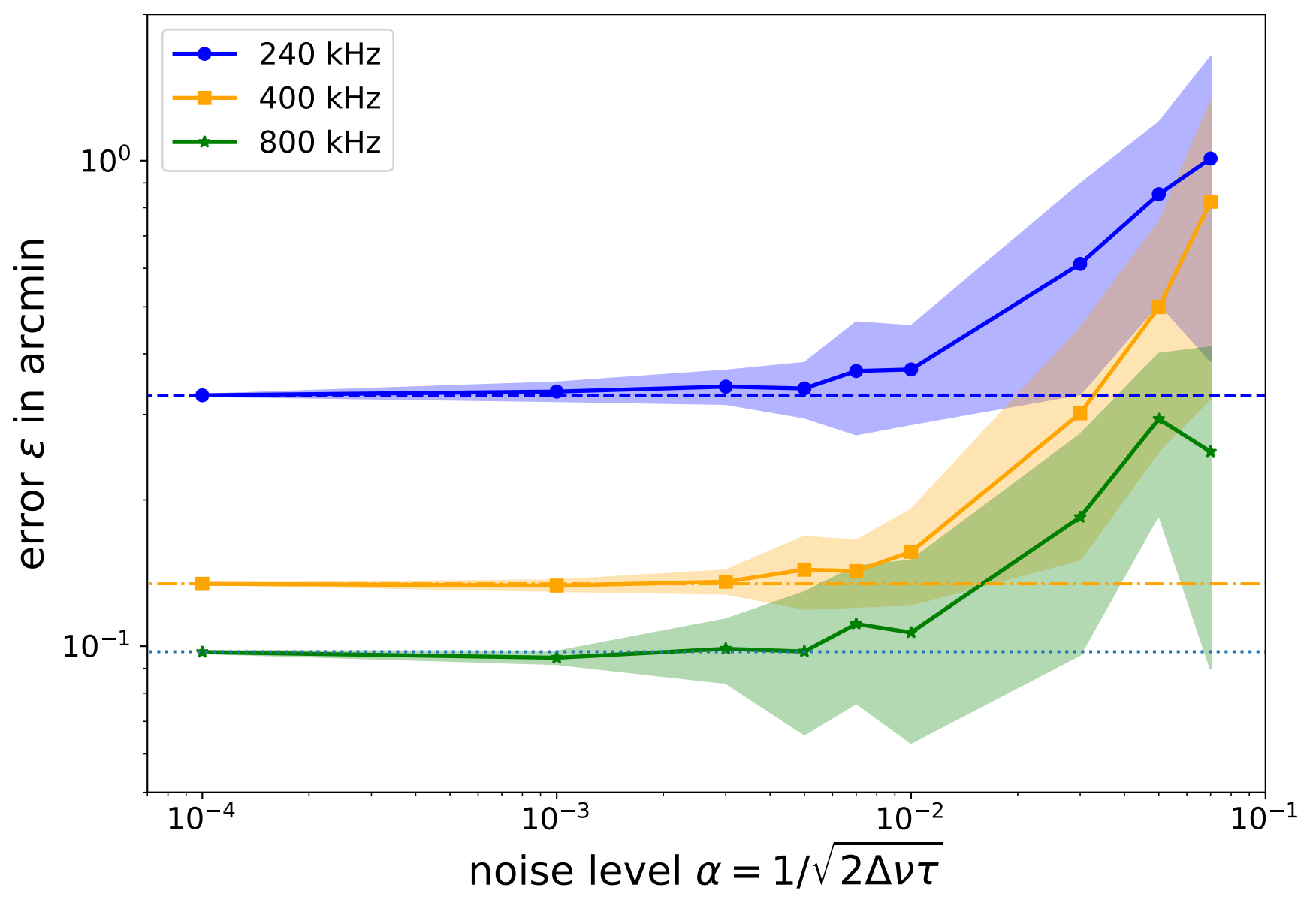
240 kHz
400 kHz
800 kHz
10^0
10^{-1}
error ε in arcmin
10^{-4}
10^{-3}
10^{-2}
10^{-1}
noise level $\alpha = 1/\sqrt{2\Delta\nu\tau}$

Figure 11.

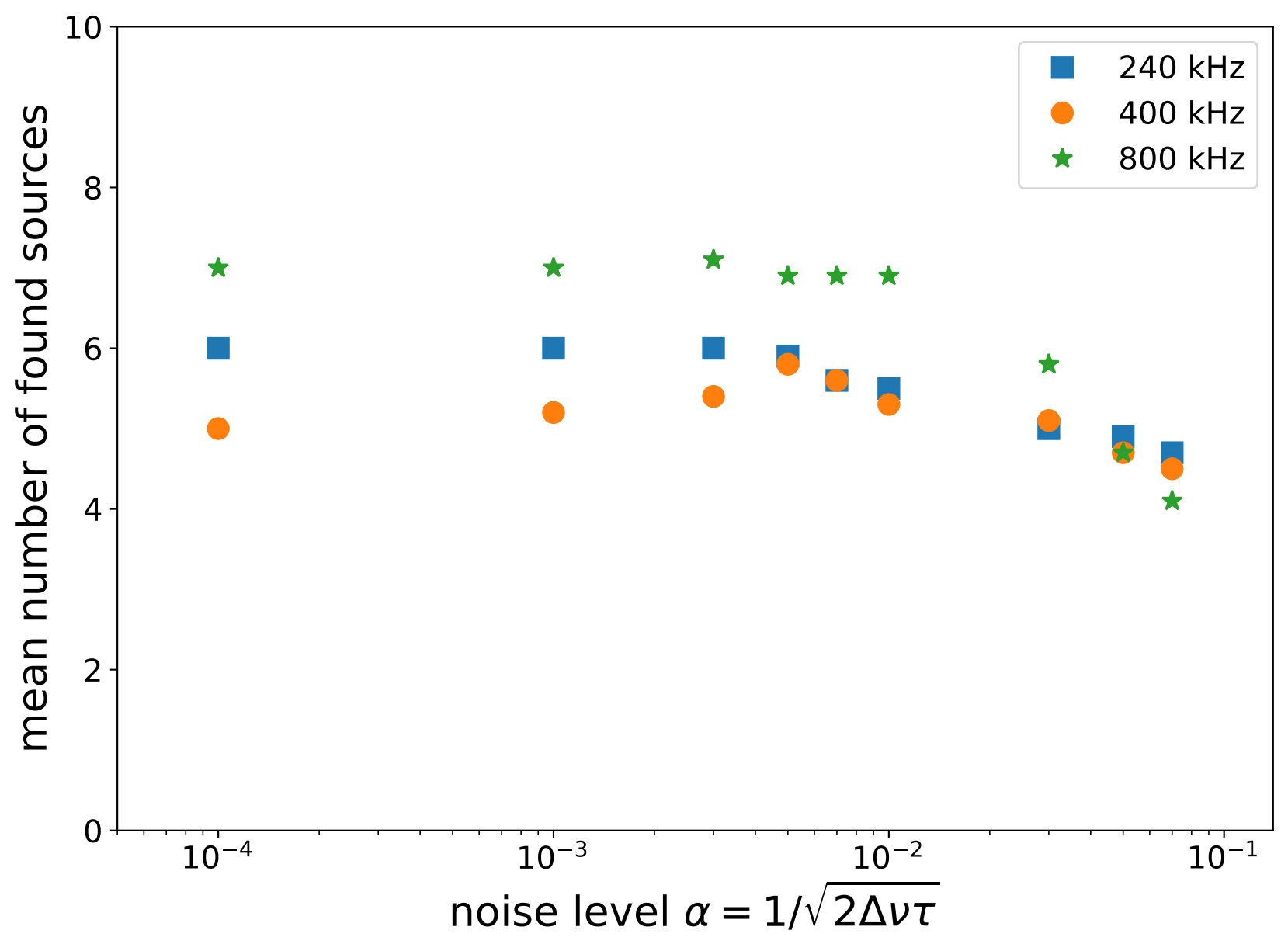
240 kHz
400 kHz
800 kHz
mean number of found sources
noise level $\alpha = 1/\sqrt{2\Delta\nu\tau}$
0
2
4
6
8
10
10^{-4}
10^{-3}
10^{-2}
10^{-1}

Figure 12.

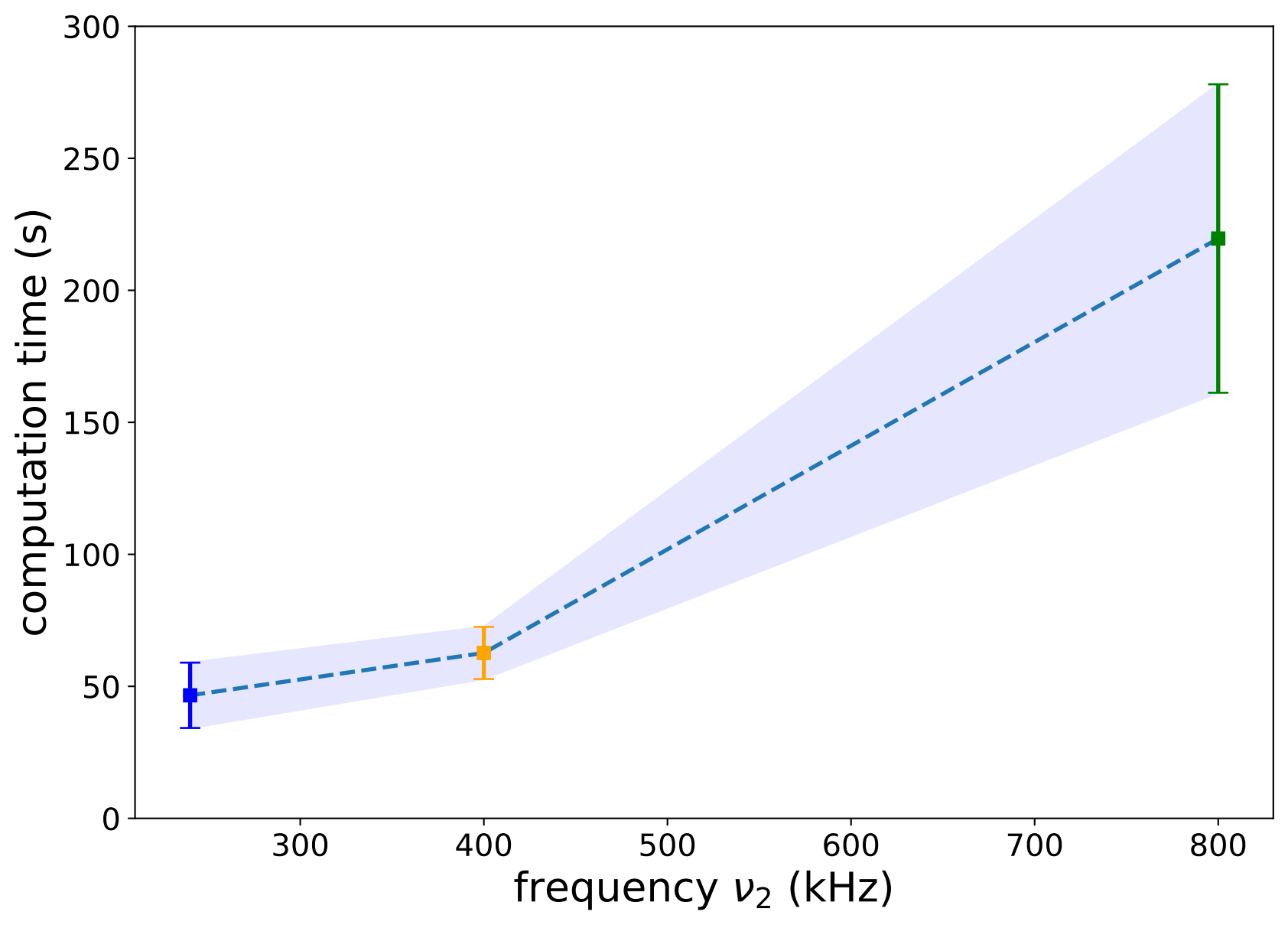
300
250
200
150
100
50
0
computation time (s)
300
400
500
600
700
800
frequency ν_2 (kHz)